J. Plasma Phys. (2025), *vol.* 91, E58 © The Author(s), 2025. Published by Cambridge University Press.
This is an Open Access article, distributed under the terms of the Creative Commons Attribution licence (https://creativecommons.org/licenses/by/4.0/), which permits unrestricted re-use, distribution and reproduction, provided the original article is properly cited. doi:10.1017/S0022377825000054

Suppression of temperature-gradient-driven turbulence by sheared flows in fusion plasmas

P.G. Ivanov[1,2], T. Adkins[2,3], D. Kennedy[4], M. Giacomin[5], M. Barnes[2,6] and A.A. Schekochihin[2,7]

[1]Ecole Polytechnique Fédérale de Lausanne (EPFL), Swiss Plasma Center (SPC), CH-1015 Lausanne, Switzerland
[2]Rudolf Peierls Centre for Theoretical Physics, University of Oxford, Oxford OX1 3PU, UK
[3]Department of Physics, University of Otago, Dunedin 9016, New Zealand
[4]United Kingdom Atomic Energy Authority, Culham Campus, Abingdon OX14 3DB, UK
[5]Dipartimento di Fisica 'G Galilei'. Università degli Studi di Padova, Padova, Italy
[6]University College, Oxford OX1 4BH, UK
[7]Merton College, Oxford OX1 4JD, UK

Corresponding author: P.G. Ivanov, plamen.ivanov@physics.ox.ac.uk

(Received 7 June 2024; revision received 9 January 2025; accepted 10 January 2025)

Starting from the assumption that saturation of plasma turbulence driven by temperature-gradient instabilities in fusion plasmas is achieved by a local energy cascade between a long-wavelength outer scale, where energy is injected into the fluctuations, and a small-wavelength dissipation scale, where fluctuation energy is thermalised by particle collisions, we formulate a detailed phenomenological theory for the influence of perpendicular flow shear on magnetised-plasma turbulence. Our theory introduces two distinct regimes, called the weak-shear and strong-shear regimes, each with its own set of scaling laws for the scale and amplitude of the fluctuations and for the level of turbulent heat transport. We discover that the ratio of the typical radial and poloidal wavenumbers of the fluctuations (i.e. their aspect ratio) at the outer scale plays a central role in determining the dependence of the turbulent transport on the imposed flow shear. Our theoretical predictions are found to be in excellent agreement with numerical simulations of two paradigmatic models of fusion-relevant plasma turbulence: (i) an electrostatic fluid model of slab electron-scale turbulence, and (ii) Cyclone-base-case gyrokinetic ion-scale turbulence. Additionally, our theory envisions a potential mechanism for the suppression of electron-scale turbulence by perpendicular ion-scale flows based on the role of the aforementioned aspect ratio of the electron-scale fluctuations.

Key words: fusion plasma, plasma nonlinear phenomena, plasma flows

1. Introduction

The quest for controlled fusion as a viable and sustainable energy source has been a long-standing scientific and engineering challenge. The performance of

https://doi.org/10.1017/S0022377825000054 Published online by Cambridge University Press

magnetic-confinement-fusion devices, such as tokamaks, is often limited by the presence of turbulent fluctuations that lead to enhanced transport and energy losses. Understanding and controlling turbulence in magnetised plasmas is therefore crucial for the success of future fusion reactors. One important aspect that has attracted considerable attention is the impact of sheared flows on the turbulence (Artun & Tang 1992; Synakowski *et al.* 1997; Waltz, Dewar & Garbet 1998; Hobbs *et al.* 2001; Mantica *et al.* 2009; McKee *et al.* 2009; Casson *et al.* 2009; Roach *et al.* 2009; Highcock *et al.* 2010; Barnes *et al.* 2011; Field *et al.* 2011; Fedorczak *et al.* 2013; Ghim *et al.* 2014; Fox *et al.* 2017; Seiferling *et al.* 2019). Such sheared flows can either be externally imposed on the turbulent fluctuations as part of the plasma equilibrium, or be self-generated by the turbulence in the form of quasistatic large-scale fluctuations known as zonal flows (Rogers, Dorland & Kotschenreuther 2000; Diamond *et al.* 2005; Dif-Pradalier *et al.* 2010, 2015; Zhu *et al.* 2020*a*,*b*; Ivanov *et al.* 2020, 2022). Sheared flows can modify the size and shape of the fluctuations, and thus have a direct impact on the transport properties of the plasma.

Despite the absence of a rigorous theory of the saturation of turbulence in magnetised plasmas, it is still possible to develop phenomenological models that, at least in some regimes, capture its essential features and allow us to make falsifiable, qualitative, and sometimes even quantitative predictions for the dependence of important turbulent properties, like the heat and particle diffusivity, on the relevant plasma parameters. Such models are often reminiscent of the original theory of hydrodynamic turbulence by Kolmogorov (1941), which posits a local energy cascade from the outer (or injection) scale – where energy is injected into turbulent fluctuations either by external forcing or by linear instabilities – through the inertial range, where the nonlinear interactions dominate the dynamics and pass the energy injected at large scales down to dissipative ones (Goldreich & Sridhar 1995; Schekochihin *et al.* 2009; Barnes *et al.* 2011; Nazarenko & Schekochihin 2011; Adkins *et al.* 2022, 2023); the energy of the fluctuations is then thermalised at these small scales, heating the plasma. The rate at which this cascade removes energy from the outer scale determines the overall turbulent amplitude and, when that is not externally imposed, the outer scale itself; in turn, the fluctuation amplitude and outer scale determine the transport. An imposed or self-generated sheared flow plays a nontrivial role in all of this.

In this article, we consider the effects of an imposed perpendicular flow shear on saturated electrostatic gyrokinetic (GK) turbulence. We first give a short recap of some relevant features of the GK framework in § 2, and then, in § 3.1, remind the reader of the standard results for saturation of such turbulence based on a local-energy-cascade phenomenology. In § 3.2, we proceed to develop a phenomenological theory of the effect of flow shear on the saturated turbulent state. The effect of this shear is to suppress the turbulent fluctuations and, in turn, the turbulent heat flux according to a certain scaling with the size of the shear. Depending on the magnitude of the imposed flow shear in comparison with the 'natural' (i.e. that in the absence of shear) rate of energy injection into the fluctuations, we distinguish weak-shear (§ 3.2.1) and strong-shear (§ 3.2.2) regimes, each with its own scaling laws for the dependence of the turbulent transport on the shear. To verify our theoretical predictions, in § 4, we present numerical results from a simple electrostatic fluid model of turbulence driven by the electron-temperature-gradient (ETG) instability (§ 4.1) and from gyrokinetic simulations of turbulence driven by the ion-temperature-gradient (ITG) instability (§ 4.2). Then, in § 5, we discuss the transport of momentum

https://doi.org/10.1017/S0022377825000054 Published online by Cambridge University Press

in the electrostatic fluid model, before finally summarising and discussing our results in § 6.

2. Gyrokinetics

We consider turbulent fluctuations in magnetised plasmas that satisfy the GK ordering $k_\perp \rho_s \sim k_\parallel L \sim 1$ and $\omega/\Omega_s \sim \rho_s/L \ll 1$, where $k_\perp$ and $k_\parallel$ are the typical perpendicular and parallel (to the mean magnetic field) wavenumbers, ρ_s and Ω_s are the Larmor radius and frequency of the charged particles of species s, ω is the inverse time scale associated with the turbulent fluctuations, and L is the length scale of variation of the plasma equilibrium. Under this ordering, we expand the distribution function for each species into equilibrium and fluctuating parts $f_s = F_s + \delta f_s$ to obtain the GK equation that governs the dynamics of the fluctuations.[1] With the additional assumption that the plasma beta $\beta_s \equiv 8\pi n_s T_s/B^2$ is small, n_s and T_s being the equilibrium density and temperature of species s, respectively, we can neglect the fluctuations of the magnetic field, leading to

$$\left(\frac{\partial}{\partial t} + \boldsymbol{u}\cdot\frac{\partial}{\partial \boldsymbol{R}_s}\right)\left(h_s - \frac{q_s\langle\phi\rangle_{\boldsymbol{R}_s}}{T_s}F_s\right) + w_\parallel \hat{\boldsymbol{b}}\cdot\frac{\partial h_s}{\partial \boldsymbol{R}_s} + \boldsymbol{v}_{ds}\cdot\frac{\partial h_s}{\partial \boldsymbol{R}_s} + \boldsymbol{v}_E\cdot\frac{\partial}{\partial \boldsymbol{R}_s}(F_s + h_s) = \sum_{s'}\langle C_{ss'}\rangle_{\boldsymbol{R}_s} \tag{2.1}$$

where the perturbed distribution function of species s is

$$\delta f_s(\boldsymbol{r}, \boldsymbol{w}) = h_s(\boldsymbol{R}_s, \varepsilon_s, \mu_s) - \frac{q_s\phi(\boldsymbol{r})}{T_s}F_s, \tag{2.2}$$

$\boldsymbol{R}_s = \boldsymbol{r} - \hat{\boldsymbol{b}}\times\boldsymbol{w}/\Omega_s$ is the gyrocentre, $\boldsymbol{w} = \boldsymbol{v} - \boldsymbol{u}$ is the peculiar velocity, $\varepsilon_s = m_s w^2/2$, $\mu_s = m_s w_\perp^2/2B$, ϕ is the perturbed electrostatic potential, F_s is the equilibrium Maxwellian distribution with density n_s and temperature T_s, $\boldsymbol{u}$ is the equilibrium plasma flow (same for all species, see Abel *et al.* 2013), the magnetic drifts are $\boldsymbol{v}_{ds} = (\hat{\boldsymbol{b}}/2\Omega_s)\times(2w_\parallel^2\hat{\boldsymbol{b}}\cdot\nabla\hat{\boldsymbol{b}} + w_\perp^2\nabla\ln B)$, the perturbed $\boldsymbol{E}\times\boldsymbol{B}$ drift is $\boldsymbol{v}_E = (c/B)\hat{\boldsymbol{b}}\times\nabla\langle\phi\rangle_{\boldsymbol{R}_s}$, $\hat{\boldsymbol{b}}$ is the unit vector parallel to the mean magnetic field, q_s is the charge of species s, $C_{ss'}$ is the linearised Fokker–Planck operator for collisions between particles of species s and s', and $\langle\ldots\rangle_{\boldsymbol{R}_s}$ denotes the standard gyroaverage. A comprehensive derivation of the GK equations can be found from, e.g. Abel *et al.* (2013) or Catto (2019). Note that the theoretical analysis presented in § 3 does not depend on a particular coordinate system, i.e. the precise choice of radial, poloidal and parallel coordinates, labelled x, y and z, respectively, will be irrelevant.

[1] Throughout this article, we use 'GK' to refer to what is commonly known as 'local, δf gyrokinetics'. Here, 'local' specifies that we are integrating (2.1) in a domain of perpendicular size that is infinitesimal in comparison with the length scale of the variation of the plasma equilibrium, and so the gradients associated with that equilibrium are taken to be constant; 'δf' means that we only consider the evolution of small-amplitude fluctuations over times that are short compared with the transport (i.e. equilibrium-variation) time scale, with the equilibrium therefore assumed constant in time.

https://doi.org/10.1017/S0022377825000054 Published online by Cambridge University Press

The nonlinear-advection and linear-drive terms in (2.1) are

$$\boldsymbol{v}_E \cdot \frac{\partial h_s}{\partial \boldsymbol{R}_s} = \frac{c}{B}\hat{\boldsymbol{b}} \cdot (\nabla x \times \nabla y) \left\{ \langle \phi \rangle_{\boldsymbol{R}_s}, h_s \right\}, \tag{2.3}$$

$$\boldsymbol{v}_E \cdot \frac{\partial F_s}{\partial \boldsymbol{R}_s} = -\frac{c}{B}\hat{\boldsymbol{b}} \cdot (\nabla x \times \nabla y) \frac{\partial \langle \phi \rangle_{\boldsymbol{R}_s}}{\partial y} \frac{\partial F_s}{\partial x}, \tag{2.4}$$

respectively, where $\{f, g\} = (\partial_x f)(\partial_y g) - (\partial_y f)(\partial_x g)$. The nonlinear term (2.3) expresses the advection of the perturbed distribution function by the perturbed $\boldsymbol{E} \times \boldsymbol{B}$ flow, while the linear term (2.4) represents the injection of free energy by the radial gradients of the equilibrium (via the advection of that equilibrium by the perturbed flows). The electrostatic GK equation is closed by the quasineutrality condition:

$$\sum_s q_s \int \mathrm{d}^3 \boldsymbol{w}\, \delta f_s = 0, \tag{2.5}$$

where the velocity integral is evaluated at fixed $\boldsymbol{r}$.

Finally, fluctuations that evolve according to (2.1) can be shown to satisfy a free-energy conservation law (Abel *et al.* 2013) of the form

$$\frac{\mathrm{d}W}{\mathrm{d}t} = I - D, \tag{2.6}$$

where the free-energy density W in a plasma of volume V is given by

$$W = \sum_s \int \frac{\mathrm{d}^3 \boldsymbol{r}}{V} \int \mathrm{d}^3 \boldsymbol{w}\, \frac{T_s \delta f_s^2}{2F_s}. \tag{2.7}$$

The dissipation D in (2.6) arises due to particle collisions and is a sink of free energy. Its precise form will not be needed here. The free-energy injection rate I depends on the gradients of the equilibrium distribution F_s and can be written as[2]

$$I = -\sum_s \left[\Gamma_s T_s \left(\frac{\partial \ln n_s}{\partial x} - \frac{3}{2}\frac{\partial \ln T_s}{\partial x} \right) + Q_s \frac{\partial \ln T_s}{\partial x} \right], \tag{2.8}$$

where we have defined the flux of particles Γ_s and the heat (or energy) flux Q_s due to species s as

$$\Gamma_s \equiv \int \frac{\mathrm{d}^3 \boldsymbol{r}}{V} \int \mathrm{d}^3 \boldsymbol{w}\, (\boldsymbol{v}_E \cdot \nabla x) \delta f_s, \tag{2.9}$$

$$Q_s \equiv \int \frac{\mathrm{d}^3 \boldsymbol{r}}{V} \int \mathrm{d}^3 \boldsymbol{w}\, (\boldsymbol{v}_E \cdot \nabla x) \frac{m_s v^2}{2} \delta f_s. \tag{2.10}$$

In the most general case, I depends on both fluxes and can be estimated as

$$I \sim \frac{\Gamma_s T_s}{L_{n_s}} \sim \frac{Q_s}{L_{T_s}}, \tag{2.11}$$

[2]Strictly speaking, (2.8) contains another injection term that is associated with the radial gradient of $\boldsymbol{u}$. Here, we assume that this can be neglected (see also footnote 5).

https://doi.org/10.1017/S0022377825000054 Published online by Cambridge University Press

where no additional orderings have been imposed on the density $L_{n_s}^{-1} \equiv -\partial_x \ln n_s$ and the temperature $L_{T_s}^{-1} \equiv -\partial_x \ln T_s$ gradients, *viz.* $L_{n_s} \sim L_{T_s} \sim L$. In this work, we consider only temperature-gradient-driven instabilities in cases where $\Gamma_s = 0$ and so our main focus will be on Q_s. Nevertheless, the arguments presented in § 3 are readily generalisable to cases where the injection of energy is dominated by the particle flux rather than the heat flux.

3. Nonlinear saturation

Magnetised-plasma turbulence exhibits a broad range of different saturation mechanisms and so a universal theory of turbulent saturation under the influence of flow shear is not feasible. Instead, here we focus on one particular type of saturated state, *viz.* that for which the following two assumptions hold: (i) there is a scale separation between the energy-injection scale (the *outer scale*), where linear instabilities inject free energy into the fluctuations, and the *dissipation scale*, where fluctuations lose energy to dissipative effects (*viz.,* ultimately, particle collisions); and (ii) the transfer of energy between these scales is realised by a local (in scale) energy cascade. This allows us to define the *inertial range* as the range of scales between the outer and dissipation scales where the local energy cascade takes place. Let us revisit the current understanding of how such an energy cascade determines the properties of the saturated turbulence.

3.1. *Outer scale, free-energy cascade and turbulent heat flux*

The form of the GK nonlinearity (2.3) implies that the nonlinear time $\tau_{\rm nl}$ at poloidal scale k_y satisfies

$$\tau_{\rm nl}^{-1} \sim \Omega_s \rho_s^2 k_x k_y \overline{\varphi}, \tag{3.1}$$

where $\overline{\varphi}$ is a measure of the characteristic amplitude of the normalised electrostatic potential $\varphi \equiv q_s\phi/T_s$ at scale k_y and s is any reference particle species. In (3.1), the radial scale k_x is an implicit function of k_y, *viz.* at each k_y, the turbulent fluctuations have a typical radial scale k_x that depends on k_y. With this in mind, (3.1) can also be written as

$$\tau_{\rm nl}^{-1} \sim \mathcal{A}\Omega_s \rho_s^2 k_y^2 \overline{\varphi}, \tag{3.2}$$

where we have defined the *fluctuation aspect ratio* at scale k_y as $\mathcal{A} \equiv k_x/k_y$. This aspect ratio will play a critical role in the theory of sheared turbulence laid out in § 3.2. Note that the precise definition of $\overline{\varphi}$ is not important because the phenomenological theory that is to follow predicts only scalings; nevertheless, to make things specific, one possible such definition is

$$\overline{\varphi}^2 \equiv \int_{|k_y'|>k_y} \mathrm{d}k_y' \int_{-\infty}^{+\infty} \mathrm{d}k_x' \int \frac{\mathrm{d}z}{L_\parallel} |\varphi_{\boldsymbol{k}_\perp'}|^2, \tag{3.3}$$

where $\varphi_{\boldsymbol{k}_\perp}$ is the two-dimensional spatial Fourier transform of φ in x and y, i.e. in the plane perpendicular to the equilibrium magnetic field, and $L_\parallel$ is the parallel size of the integration domain of (2.1) (assumed finite). By Parseval's theorem, the contributions to the free energy (2.7) at each scale are proportional to the squared amplitude of the fluctuations and so, in view of (2.2) and (2.5), to $\overline{\varphi}^2$.

https://doi.org/10.1017/S0022377825000054 Published online by Cambridge University Press

If $k_x \sim k_y \sim k_\perp$ (i.e. $\mathcal{A} \sim 1$) is satisfied throughout the inertial range, (3.1) implies that the free-energy flux ε through scale $k_\perp$ satisfies[3]

$$\varepsilon \sim \tau_{\rm nl}^{-1} n_s T_s \overline{\varphi}^2 \propto k_\perp^2 \overline{\varphi}^3, \tag{3.4}$$

where $\mathrm{d}/\mathrm{d}t \sim \tau_{\rm nl}^{-1}$ in the inertial range because the dynamics there is dominated by the nonlinear effects. Assuming a local, constant-flux cascade, *viz.* that ε is constant throughout the inertial range, and using (3.1), we conclude that

$$\overline{\varphi} \propto k_\perp^{-2/3} \implies \tau_{\rm nl}^{-1} \propto k_\perp^{4/3} \tag{3.5}$$

in the inertial range. The assumption that $\mathcal{A} \sim 1$ in the inertial range is motivated by the fact that the nonlinearity in (2.1) is isotropic in the perpendicular plane. However, this is not a sufficient condition for $\mathcal{A} \sim 1$. For example, reduced magnetohydrodynamic (RMHD) turbulence, whose nonlinearity is also isotropic in the plane perpendicular to the mean magnetic field, is known to have fluctuations that are anisotropic in the perpendicular plane and whose anisotropy depends on the scale, thus introducing a nontrivial scale-dependent factor into the RMHD version of (3.1) (Boldyrev 2006; Boldyrev, Mason & Cattaneo 2009; Mallet *et al.* 2016; Mallet & Schekochihin 2017; Schekochihin 2022). Nevertheless, assuming $\mathcal{A} \sim 1$ in the inertial range is not unreasonable and it agrees with our numerical observations reported in § 4.

Assuming that the rate of energy injection is determined by the linear-instability growth rate $\gamma_{\boldsymbol{k}}$ and that the latter satisfies $\gamma_{\boldsymbol{k}} \propto k_y$,[4] the inertial-range nonlinear rate (3.5) has a steeper dependence on k_y than the injection rate. The outer scale will then be the scale at which the rates of nonlinear mixing and linear injection balance (Barnes *et al.* 2011; Adkins *et al.* 2022, 2023):

$$\left(\tau_{\rm nl}^{\rm o}\right)^{-1} \sim \gamma^{\rm o}. \tag{3.6}$$

Here and in what follows, the superscript '$^{\rm o}$' denotes quantities associated with the outer scale. The inertial range is thus located at $k_y > k_y^{\rm o}$, where the nonlinear interactions dominate the linear injection rate (see figure 1).

3.1.1. Heat flux

Assuming that the heat flux Q_s is dominated by contributions from the outer scale, we can estimate it, in view of its definition (2.10), as follows:

$$Q_s \sim Q_s^{\rm o} \sim n_s T_s v_{{\rm th}s} k_y^{\rm o} \rho_s \left(\overline{\varphi}^{\rm o}\right)^2. \tag{3.7}$$

[3] In general, (2.6) implies that $\varepsilon \sim I$. However, the free-energy flux need not equal the injection rate exactly. One such example is the fluid model of ETG turbulence described in § 4.1, whose free-energy-injection mechanism relies on finite collisional dissipation due to the nature of the linear instability and thus a certain order-unity fraction of I is directly dissipated at the outer scale (Adkins *et al.* 2023).

[4] Note that, for every k_y, there may be many unstable modes. For instance, in the 'slab' geometry, where the linear modes are parametrised by the radial k_x and parallel $k_\parallel$ wavenumbers, there exists a broad spectrum of unstable modes for any given k_y. The relation $\gamma_{\boldsymbol{k}} \propto k_y$ does not refer to the growth rate of one particular mode (in the slab case, that would be a mode with fixed k_x and $k_\parallel$), but rather to the growth rate of a mode that is chosen by maximising the growth rate with respect to k_x and $k_\parallel$ at that particular k_y. This relation is exact for long-wavelength electrostatic instabilities with $k_\perp \rho_s \ll 1$, where the outer scale of GK turbulence often resides. In this limit, (2.1) asymptotes to the electrostatic drift-kinetic equation, and, in the slab geometry, $\gamma_{\boldsymbol{k}} \propto k_y$ follows from the scale invariance of drift kinetics (Adkins *et al.* 2023).

https://doi.org/10.1017/S0022377825000054 Published online by Cambridge University Press

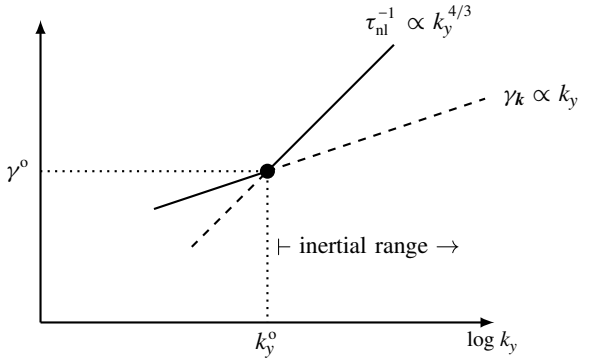


FIGURE 1. An illustration of the relationship between the nonlinear mixing rate $\tau_{\rm nl}^{-1}$, the energy-injection rate $\gamma_{\boldsymbol{k}}$ and the location of the outer scale, where $\tau_{\rm nl}^{-1} \sim \gamma_{\boldsymbol{k}}$. The scaling $\tau_{\rm nl}^{-1} \propto k_y^{4/3}$ is a consequence of the local energy cascade and is thus valid only in the inertial range $k_y > k_y^{\rm o}$ (see the discussion in § 3.1).

This is justified as long as the spectrum of the fluctuations decays sufficiently quickly in the inertial range; specifically, we require the fluctuation amplitudes to decay faster than $k_\perp^{-1/2}$, which is readily satisfied by (3.5). We also assume that the phase relationship between φ and δf_s does not introduce any nontrivial factors – technically, (3.7) is an upper bound for (2.10). Using (3.2) and (3.6), we can rewrite (3.7) as

$$\frac{Q_s}{n_s T_s v_{{\rm th}s}} \sim \left(\frac{\gamma^{\rm o}}{\Omega_s}\right)^2 \frac{1}{(k_y^{\rm o}\rho_s)^3 (\mathcal{A}^{\rm o})^2}. \tag{3.8}$$

Therefore, to determine Q_s, we need to know the energy-injection rate $\gamma^{\rm o}$ (or equivalently $\tau_{\rm nl}^{\rm o}$), the poloidal wavenumber $k_y^{\rm o}$ and the fluctuation aspect ratio $\mathcal{A}^{\rm o}$ at the outer scale. If $\gamma^{\rm o} \sim \gamma_{\boldsymbol{k}^{\rm o}}$, where $\gamma_{\boldsymbol{k}^{\rm o}}$ is the growth rate at the outer scale, then only two of $\gamma^{\rm o}$, $k_y^{\rm o}$ and $\mathcal{A}^{\rm o}$ are independent. Thus, we require additional assumptions. There are multiple ways to proceed.

In the absence of flow shear, Barnes *et al.* (2011) posit: (i) that the outer scale is governed by the 'critical balance' of $\gamma^{\rm o}$ and $(\tau_{\rm nl}^{\rm o})^{-1}$ with the parallel-streaming rate across the plasma connection length, $\omega_\parallel^{\rm o} \sim v_{{\rm th}s}/qR$, where q and R are the safety factor and major radius, respectively; (ii) that the outer-scale fluctuations are isotropic, $\mathcal{A}^{\rm o} \sim 1$; and (iii) that the energy-injection rate is given by a simple estimate of the growth rate of temperature-gradient-driven instabilities, $\gamma^{\rm o} \sim k_y^{\rm o}\rho_s v_{{\rm th}s}/L_{T_s}$. Combined with (3.8), assumptions (i)–(iii) imply

$$\frac{Q_s}{n_s T_s v_{{\rm th}s}} \sim \left(\frac{\rho_s}{R}\right)^2 \left(\frac{R}{L_{T_s}}\right)^3 q. \tag{3.9}$$

Note that Barnes *et al.* (2011) studied ion-scale turbulence, which amounts to setting $s = i$ in the above arguments.

A modification of these results, backed by experimental (Ghim *et al.* 2013) and theoretical (Nies *et al.* 2024) evidence, is to replace assumption (ii) in the arguments by Barnes *et al.* (2011) by a 'grand critical balance'

$$\gamma^{\rm o} \sim (\tau_{\rm nl}^{\rm o})^{-1} \sim \omega_\parallel^{\rm o} \sim \omega_{d,x}^{\rm o} \tag{3.10}$$

https://doi.org/10.1017/S0022377825000054 Published online by Cambridge University Press

between all the aforementioned rates and the radial magnetic-drift frequency $\omega^{\mathrm{o}}_{d,x} \sim k^{\mathrm{o}}_x \rho_s v_{\mathrm{th}s}/R$ at the outer scale. This implies

$$\mathcal{A}^{\mathrm{o}} \sim \frac{R}{L_{T_s}}, \tag{3.11}$$

which, together with (3.8), results in the following scaling for the heat flux:

$$\frac{Q_s}{n_s T_s v_{\mathrm{th}s}} \sim \left(\frac{\rho_s}{R}\right)^2 \frac{R}{L_{T_s}} q. \tag{3.12}$$

In the rest of this paper, we consider the influence of mean flow shear on the saturated state. We will not discuss the details of how the outer scale is determined in the case of zero imposed flow shear, but assume that the system does indeed have a well-defined zero-shear saturated state, that the outer-scale nonlinear rate is governed by (3.2) and (3.6), and that (3.8) is a good estimate for the heat flux. Thus, our arguments will hold regardless of whether the zero-shear outer scale is chosen à la Barnes *et al.* (2011), through a grand critical balance, or otherwise.

3.2. *Perpendicular flow shear*

For the remainder of this article, we assume an equilibrium shear flow in the direction perpendicular to the mean magnetic field and with a linear profile: $\boldsymbol{u} = \gamma_E x \hat{\boldsymbol{y}}$, where γ_E is the shearing rate.[5] In the presence of such a flow, the GK equation (2.1) is no longer homogeneous in x. For brevity, we henceforth drop the species subscript from the heat flux Q.

To understand the effect of the flow shear on the fluctuations, it is instructive to consider a patch of turbulence in which the magnetic field can be considered locally constant and oriented along the z-direction; i.e. this patch is approximated as a 'slab'. One can then perform a coordinate transformation from the original (*laboratory*) frame to the so-called *shearing frame* (Newton, Cowley & Loureiro 2010; Schekochihin, Highcock & Cowley 2012):

$$t' = t, \;\; x' = x, \;\; y' = y - x\gamma_E t, \;\; z' = z. \tag{3.13}$$

The substitution of (3.13) into the GK equation (2.1) eliminates the radially inhomogeneous advection term $\boldsymbol{u} \cdot \boldsymbol{\nabla}$ at the cost of introducing an inhomogeneity in time via the ∂_x derivatives. Consequently, the laboratory-frame radial wavenumber k_x of a fluctuation advected by the mean flow, i.e. of a fluctuation with a given fixed wavenumber $\boldsymbol{k}'$ in the shearing frame, satisfies

$$k_x = k'_x - k'_y \gamma_E t'. \tag{3.14}$$

Crucially, the nonlinear interactions (2.3) and the linear drive (2.4) have the same form in both the laboratory frame and the shearing frame; therefore, (3.14) captures

[5] In general, a pure perpendicular linear shear is not realistic: e.g. $\boldsymbol{u}$ is purely toroidal in axisymmetric devices and hence has a component parallel to the mean magnetic field (Abel *et al.* 2013). For certain equilibria, the radial gradient of the parallel component of the mean flow can act as a source of energy, resulting in the so-called parallel-velocity-gradient (PVG) instability (Catto, Rosenbluth & Liu 1973; Newton *et al.* 2010; Schekochihin *et al.* 2012). Here, we assume that there is no PVG instability (or at least that it is irrelevant for the saturated state, which is reasonable if the shear is not too large; Highcock *et al.* 2010; Barnes *et al.* 2011) and ignore the shear in the parallel velocity.

https://doi.org/10.1017/S0022377825000054 Published online by Cambridge University Press

completely the effects of flow shear in the shearing frame. Equation (3.14) tells us that the shearing action of the perpendicular flow, which results in a 'tilting' of the eddies (Fox *et al.* 2017), is equivalent to a 'drift' in Fourier space of the radial wavenumber k_x of the turbulent fluctuations.

Let us consider introducing flow shear into a system that, in its absence, would reach a saturated state by establishing a local energy cascade. As discussed in § 3.1, the transport properties (e.g. the radial heat flux Q) of such a system are dominated by the fluctuations at the outer scale. The lifetime of these fluctuations is given by the outer-scale nonlinear time, which, according to (3.6), is $\tau_{\rm nl}^{\rm o}(0) \sim \gamma^{\rm o}(0)^{-1}$, where we will use the notation $\gamma^{\rm o}(\gamma_E)$ to denote the dependence of outer-scale quantities on the flow shear, so $\gamma^{\rm o}(0)$ is the outer-scale injection rate in the absence of it. We shall distinguish two different regimes of sheared turbulence: a *weak-shear regime* with $\gamma_E < \gamma^{\rm o}(0)$ and a *strong-shear regime* with $\gamma_E > \gamma^{\rm o}(0)$. This distinction is motivated by the so-called 'quench' rule (Waltz, Kerbel & Milovich 1994, 1998; Kobayashi & Rogers 2012; Ivanov *et al.* 2020), according to which flow shear is able to suppress the energy injection associated with some linearly unstable modes only if the shearing rate is comparable to the growth rate of those modes. If this is true, the flow shear should be unable to stifle energy injection at the outer scale if $\gamma_E < \gamma^{\rm o}(0)$ and so the outer-scale injection rate should remain independent of γ_E in the weak-shear regime, i.e. $\gamma^{\rm o}(\gamma_E) \approx \gamma^{\rm o}(0)$. In contrast, in the strong-shear regime, we expect that the injection rate will be modified by the presence of the flow shear.

Let us analyse the physics of both regimes, starting with the weak-shear one.

3.2.1. Weak-shear regime

Let us consider more carefully the influence of flow shear on the outer scale in the case $\gamma_E < \gamma^{\rm o}(0)$. As just discussed, in this regime, the outer-scale-injection and nonlinear-mixing rates should remain approximately the same as those at $\gamma_E = 0$, *viz.*

$$\tau_{\rm nl}^{\rm o}(\gamma_E)^{-1} \sim \gamma^{\rm o}(\gamma_E) \sim \gamma^{\rm o}(0) \sim \tau_{\rm nl}^{\rm o}(0)^{-1}. \tag{3.15}$$

Assuming that the injection rate $\gamma^{\rm o}$ is determined by the linear growth rate at the outer scale[6] and that the latter is (at least approximately) only a function of k_y,[7] we conclude that the poloidal wavenumber of the outer-scale eddies is also set by its value at $\gamma_E = 0$ and independent of γ_E in the weak-shear regime, *viz.*

$$k_y^{\rm o}(\gamma_E) \sim k_y^{\rm o}(0). \tag{3.16}$$

However, the assumption that $\gamma_{\boldsymbol{k}}$ is only a weak function of k_x means that one cannot make a similar statement about the radial wavenumber $k_x^{\rm o}(\gamma_E)$. Indeed,

[6]Strictly speaking, linear modes in the presence of flow shear are often only transiently growing, so $\gamma^{\rm o}(\gamma_E)$ should be interpreted as the transient growth rate at early times (Highcock *et al.* 2011; Schekochihin *et al.* 2012). We also note that a shear in the equilibrium magnetic field can introduce nontrivial effects, e.g. travelling exponentially growing modes (Newton *et al.* 2010) or non-exponentially growing Floquet modes (Cooper 1988; Waelbroeck & Chen 1991), which can have a significant impact on the saturation, e.g. they may lead to a bistable saturated state (Christen *et al.* 2022). Our analysis depends only on the injection rate being a function solely of the poloidal wavenumber, while the precise relationship between the injection rate and the linear growth rate is outside of the scope of the current work.

[7]This assumption can be made weaker: we will only need $\gamma_{\boldsymbol{k}}$ to be approximately independent of k_x for $k_x < k_y$.

https://doi.org/10.1017/S0022377825000054 Published online by Cambridge University Press

approximating the lifetime of the outer-scale fluctuations as equal to the nonlinear mixing time $\tau_{\rm nl}^{\rm o}$, the wavenumber drift (3.14), together with (3.15) and (3.16), suggests that

$$k_x^{\rm o}(\gamma_E) \sim k_x^{\rm o}(0) + k_y^{\rm o}(0)\tau_{\rm nl}^{\rm o}(0)\gamma_E \sim k_x^{\rm o}(0)\left[1 + \frac{\gamma_E}{\mathcal{A}^{\rm o}(0)\gamma^{\rm o}(0)}\right], \tag{3.17}$$

where $\mathcal{A}^{\rm o}(0) = k_x^{\rm o}(0)/k_y^{\rm o}(0)$ is the fluctuation aspect ratio at the outer scale at $\gamma_E = 0$. Therefore,

$$\frac{k_x^{\rm o}(\gamma_E)}{k_x^{\rm o}(0)} \sim \frac{\mathcal{A}^{\rm o}(\gamma_E)}{\mathcal{A}^{\rm o}(0)} \sim 1 + \frac{\gamma_E}{\gamma_{\rm c}}, \tag{3.18}$$

where we have introduced the *critical shearing rate*

$$\gamma_{\rm c} \equiv \mathcal{A}^{\rm o}(0)\gamma^{\rm o}(0). \tag{3.19}$$

Then, (3.8) implies that the radial turbulent heat flux satisfies

$$\frac{Q(\gamma_E)}{Q(0)} \sim \left[\frac{\mathcal{A}^{\rm o}(0)}{\mathcal{A}^{\rm o}(\gamma_E)}\right]^2 \sim \frac{1}{(1+\gamma_E/\gamma_{\rm c})^2}, \tag{3.20}$$

where $Q(0)$ is the heat flux at $\gamma_E = 0$. Note that at no step leading to (3.20) did we use any formulae from § 3.1 that relied on isotropy, which would otherwise have restricted us to $\mathcal{A}^{\rm o} \sim 1$. Expressions (3.19) and (3.20) predict that the transport properties in the weak-shear regime are determined by the ratio of the radial and poloidal wavenumbers of the outer-scale eddies, $\mathcal{A}^{\rm o}(0) = k_x^{\rm o}(0)/k_y^{\rm o}(0)$. If the unsheared fluctuations have $\mathcal{A}^{\rm o}(0) \sim 1$, then (3.19) implies that $\gamma_{\rm c} \sim \gamma^{\rm o}(0)$. As the weak-shear regime is characterised by $\gamma_E < \gamma^{\rm o}(0)$, (3.18) implies that $\mathcal{A}^{\rm o}(\gamma_E) \sim \mathcal{A}^{\rm o}(0) \sim 1$ and thus $Q(\gamma_E) \sim Q(0)$ throughout the weak-shear regime. In other words, if the unsheared turbulence has $\mathcal{A}^{\rm o}(0) \sim 1$ at the outer scale, shearing it with any $\gamma_E < \gamma^{\rm o}(0)$ will not reduce the turbulent transport by more than an order-unity amount – an unsurprising outcome.

However, due to the nature of the underlying linear instabilities, it is, in fact, often the case that the outer-scale eddies in temperature-gradient-driven turbulence are radially elongated. Such eddies, often called 'streamers', are a well-documented feature of this type of turbulence, especially in its electron-scale variety (Drake, Guzdar & Hassam 1988; Jenko *et al.* 2000; Dorland *et al.* 2000; Jenko 2006; Roach *et al.* 2009; Colyer *et al.* 2017). A turbulent state dominated by streamers satisfies $\mathcal{A}^{\rm o}(0) \ll 1$ and so $\gamma_{\rm c} \ll \gamma^{\rm o}(0)$. In this case, (3.18) implies that the outer-scale aspect ratio increases linearly with the flow shear due to the tilting of the eddies, *viz*.

$$\mathcal{A}^{\rm o}(\gamma_E) \sim \mathcal{A}^{\rm o}(0) + \frac{\gamma_E}{\gamma^{\rm o}(0)}. \tag{3.21}$$

Furthermore, (3.20) predicts that the heat flux will be suppressed if $\gamma_{\rm c} \lesssim \gamma_E \ll \gamma^{\rm o}(0)$. In particular, for intermediate values of the shearing rate that satisfy $\gamma_{\rm c} \ll \gamma_E \ll \gamma^{\rm o}(0)$, (3.21) becomes

$$\mathcal{A}^{\rm o}(\gamma_E) \sim \frac{\gamma_E}{\gamma^{\rm o}(0)}, \tag{3.22}$$

https://doi.org/10.1017/S0022377825000054 Published online by Cambridge University Press

and so, by (3.20),

$$Q(\gamma_E) \propto \gamma_E^{-2}. \tag{3.23}$$

If the shear is increased further, (3.21) implies that, at the transition from the weak- to the strong-shear regime, where $\gamma_E \sim \gamma^{\mathrm{o}}(0)$, the outer-scale aspect ratio is $\mathcal{A}^{\mathrm{o}}(\gamma_E) \sim 1$, and so, by (3.20), the heat flux has been reduced by a large factor:

$$\frac{Q[\gamma^{\mathrm{o}}(0)]}{Q(0)} \sim \left[\mathcal{A}^{\mathrm{o}}(0)\right]^2 \ll 1. \tag{3.24}$$

A cautious reader may have spotted a potential clash between having $\mathcal{A}^{\mathrm{o}}(0) \ll 1$ at the outer scale and the theory of the energy cascade laid out in § 3.1: there, we assumed that the fluctuations in the inertial range had $\mathcal{A} \sim 1$, yet the inertial range must connect to the outer scale, where now, $\mathcal{A} \ll 1$. There are two possible resolutions to this problem: (i) the scaling arguments presented in § 3.1 are, in fact, unchanged if the inertial range inherits the aspect ratio at the outer scale, i.e. if k_x/k_y is a scale-independent, even if numerically small, number below the outer scale; or (ii) there exists a transition region below the outer scale, wherein the dependence of k_x on k_y is faster than linear so that k_x gradually increases to match k_y at some smaller scale, below which the scalings from § 3.1 become valid. Our numerical results, presented in § 4.1, are consistent with option (ii). In Appendix A, we develop a simple theory for the transition region.

Finally, let us mention that, while here we shall consider only cases where $\mathcal{A} \lesssim 1$, this is not necessarily satisfied in all instances of fusion-relevant turbulence. For example, the large-temperature-gradient environment of the pedestal has been shown numerically to give rise to poloidally elongated turbulent fluctuations with $\mathcal{A} \gg 1$ (Parisi *et al.* 2020, 2022). As discussed in § 3.1.1, the 'grand critical balance' (3.10) leads to poloidally elongated eddies at large temperature gradients, as per (3.11). Recent numerical and analytical work by Nies *et al.* (2024) suggests that such behaviour may indeed be consistent with strongly driven ion-temperature-gradient turbulence in axisymmetric toroidal geometry. Here, leaving the reader cognisant of these recent developments, we shall nevertheless focus on the case $\mathcal{A} \lesssim 1$.

3.2.2. Strong-shear regime

In the strong-shear regime, defined by $\gamma_E > \gamma^{\mathrm{o}}(0)$, the flow shear is strong enough to affect energy injection at the outer scale. In particular, it is no longer possible to excite fluctuations at wavenumbers where the growth rate is $\gamma_{\boldsymbol{k}} \lesssim \gamma_E$ (Waltz *et al.* 1994, 1998). To compensate for this, the outer scale must adjust to match the shearing rate. Thus, we propose that, for $\gamma_E \gg \gamma^{\mathrm{o}}(0)$, the outer scale will be governed by the balance of nonlinear, injection and shearing rates:

$$\tau_{\mathrm{nl}}^{\mathrm{o}}(\gamma_E)^{-1} \sim \gamma^{\mathrm{o}}(\gamma_E) \sim \gamma_E, \tag{3.25}$$

as illustrated in figure 2. As always, the lifetime of turbulent eddies at the outer scale is set by the nonlinear time; (3.14) then implies that $\mathcal{A}^{\mathrm{o}}(\gamma_E) \sim 1$ throughout the strong-shear regime. Assuming that the linear growth rate is $\gamma_{\boldsymbol{k}} \propto k_y$, we expect that

$$k_y^{\mathrm{o}} \propto \gamma_E. \tag{3.26}$$

https://doi.org/10.1017/S0022377825000054 Published online by Cambridge University Press

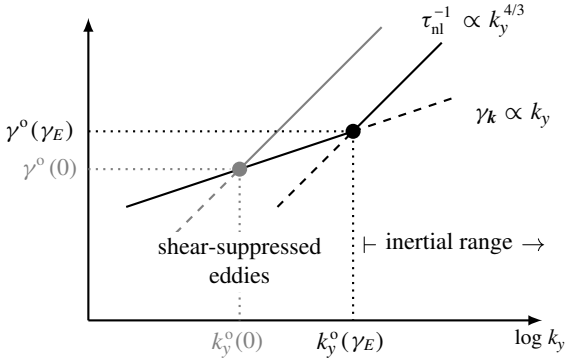


FIGURE 2. A qualitative illustration, analogous to figure 1, of the effect of strong flow shear $\gamma_E \gg \gamma^{\rm o}(0)$, leading to the time scale balance (3.25) determining the outer scale. In this regime, $\gamma^{\rm o}(\gamma_E) \sim \gamma_E$.

This is intuitively clear: stronger flow shear pushes turbulence towards smaller (and thus faster) scales since the larger (and slower) eddies are more strongly affected by the shear. Consequently, (3.8), together with (3.25) and (3.26), implies

$$Q(\gamma_E) \propto \gamma_E^{-1} \tag{3.27}$$

in the strong-shear regime $\gamma_E > \gamma^{\rm o}(0)$.

The outer-scale balance (3.25), and thus the scaling (3.27), cannot be satisfied for arbitrarily large values of flow shear because the linear growth rate $\gamma_{\boldsymbol{k}}$ is bounded by some $\gamma_{\rm max}$, normally found at much larger wavenumbers than those associated with the dominant energy injection.[8] For $\gamma_E \gtrsim \gamma_{\rm max}$, the system is no longer able to sustain the turbulent fluctuations because the shearing rate γ_E cannot be matched by the rate of energy injection at *any* scale. Therefore, we expect a sharp cut-off in the fluctuations' amplitude, and thus in the heat flux, as γ_E becomes comparable to $\gamma_{\rm max}$. Figure 3 summarises the expected dependence of the heat flux on γ_E in both regimes.

4. Numerical results

To test the validity of the theory presented in § 3.2, we consider two different models of turbulence. The first (§ 4.1) is a two-fluid model that captures the dynamics of electrostatic fluctuations of density and electron temperature in a straight magnetic field. This turbulence is driven by the collisional slab ETG (sETG) instability (Adkins *et al.* 2022) on scales between the ion and electron gyroradii. While this model is extremely simple, even simplistic, the benefit of using it is that its saturation mechanism has already been investigated in great detail and has been shown to conform to the picture of a local energy cascade outlined in § 3.1 (Adkins, Ivanov & Schekochihin 2023). Therefore, it is a prime candidate for confirming the validity of the theory laid out in this paper. For our second set of simulations (§ 4.2), we employ the GK code GENE (Jenko *et al.* 2000; Jenko 2000) to perform gyrokinetic flux-tube simulations of ITG-driven turbulence. This is a much more realistic model

[8]The existence of such $\gamma_{\rm max}$ can be proven rigorously in some cases, e.g. ion-temperature-gradient-driven turbulence with adiabatic electrons (Helander & Plunk 2022).

https://doi.org/10.1017/S0022377825000054 Published online by Cambridge University Press

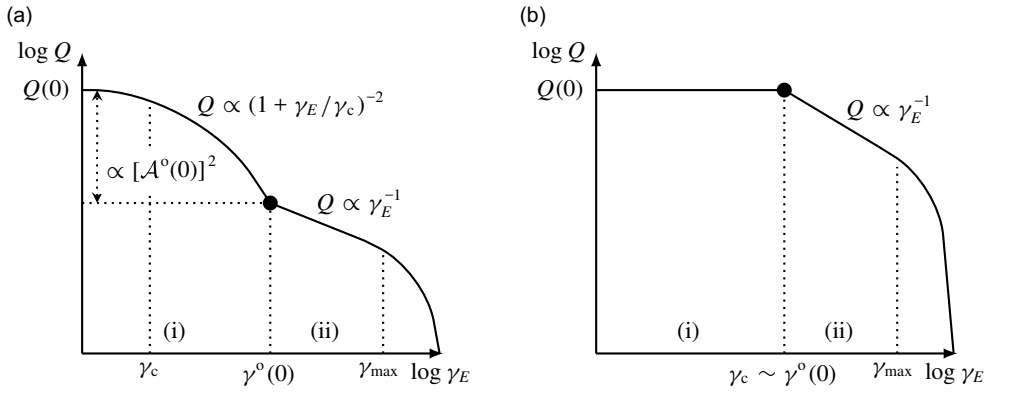


FIGURE 3. A qualitative diagram of the heat flux Q as a function of the flow shear γ_E in the case of (*a*) $\mathcal{A}^{\rm o}(0) \ll 1$ and (*b*) $\mathcal{A}^{\rm o}(0) \sim 1$. In each case, there are two distinct regimes. (i) For $\gamma_E < \gamma^{\rm o}(0)$, we have the weak-shear regime (§ 3.2.1), where, in the $\mathcal{A}^{\rm o}(0) \ll 1$ case, we find $Q(\gamma_E) \propto (1+\gamma_E/\gamma_{\rm c})^{-2}$ [see (3.20)]. In contrast, if $\mathcal{A}^{\rm o}(0) \sim 1$, the flow shear is unable to affect significantly the fluctuations at the outer scale and, consequently, the heat flux is approximately independent of γ_E. (ii) For $\gamma^{\rm o}(0) < \gamma_E < \gamma_{\rm max}$, the system is in the strong-shear regime (§ 3.2.2), where the outer-scale injection rate is determined by the flow shear, *viz.* $\gamma^{\rm o}(\gamma_E) \sim \gamma_E$. Here, $\mathcal{A}^{\rm o}(\gamma_E) \sim 1$ at the outer scale, regardless of $\mathcal{A}^{\rm o}(0)$, and $Q(\gamma_E) \propto \gamma_E^{-1}$. Finally, the fluctuations, and hence the heat flux, are completely suppressed at $\gamma_E \gtrsim \gamma_{\rm max}$.

of plasma turbulence, and the 'Cyclone base case' used here is a setup that has been extensively studied in the literature (Lin *et al.* 1999; Dimits *et al.* 2000; Barnes *et al.* 2009; Highcock *et al.* 2012; Peeters *et al.* 2016; Li *et al.* 2021; C. J. *et al.* et al., 2021; Volčokas *et al.* 2022; Hoffmann, Frei & Ricci 2023; Lippert, Rath & Peeters 2023; Tirkas *et al.* 2023 constitute a small sample) – it is thus a natural testbed for any theory aspiring to tokamak relevance.

4.1. *Fluid ETG turbulence*

In this section, we report numerical simulations in a triply periodic domain of size L_x, L_y and $L_\parallel$ in x, y and z, respectively, of the following collisional slab ETG model (Adkins *et al.* 2023):

$$\frac{\mathrm{d}}{\mathrm{d}t}\frac{\delta n_e}{n_e} + \frac{\partial u_{\parallel e}}{\partial z} = 0, \tag{4.1}$$

$$\frac{\nu_{ei}}{c_1}\frac{u_{\parallel e}}{v_{\mathrm{the}}} = -\frac{v_{\mathrm{the}}}{2}\frac{\partial}{\partial z}\left[\frac{\delta n_e}{n_e} - \varphi + \left(1+\frac{c_2}{c_1}\right)\frac{\delta T_e}{T_e}\right], \tag{4.2}$$

$$\frac{\mathrm{d}}{\mathrm{d}t}\frac{\delta T_e}{T_e} - \frac{c_3 v_{\mathrm{the}}^2}{3\nu_{ei}}\frac{\partial^2}{\partial z^2}\frac{\delta T_e}{T_e} + \frac{2}{3}\left(1+\frac{c_2}{c_1}\right)\frac{\partial u_{\parallel e}}{\partial z} = -\frac{\rho_e v_{\mathrm{the}}}{2L_T}\frac{\partial \varphi}{\partial y}, \tag{4.3}$$

where the 'convective derivative'

$$\frac{\mathrm{d}}{\mathrm{d}t} = \frac{\partial}{\partial t} + \gamma_E x\frac{\partial}{\partial y} + \frac{\rho_e v_{\mathrm{the}}}{2}\left(\hat{\boldsymbol{z}}\times\boldsymbol{\nabla}\varphi\right)\cdot\boldsymbol{\nabla} + \nu_\perp \rho_e^4 \nabla_\perp^4 \tag{4.4}$$

includes the mean flow shear, the nonlinear advection by the perturbed $\boldsymbol{E}\times\boldsymbol{B}$ drift and hyperviscous dissipation. Appendix B describes some important details of the

https://doi.org/10.1017/S0022377825000054 Published online by Cambridge University Press

numerical implementation of the flow-shearing term $\gamma_E x\partial_y$. The electron density is related to the electrostatic potential $\varphi \equiv e\phi/T_e$ by quasineutrality (2.5) combined with the assumption of adiabatic ions:

$$\frac{\delta n_e}{n_e} = -\frac{ZT_e}{T_i}\varphi, \tag{4.5}$$

where $Z = q_i/e$, q_i being the ion charge. The numerical coefficients c_1, c_2 and c_3 arise from the physics of collisions and depend on Z: e.g. for $Z = 1$, $c_1 \approx 1.94$, $c_2 \approx 1.39$ and $c_3 \approx 3.16$, in agreement with Braginskii (1965). We used $Z = 1$ and $T_i = T_e$ for all simulations reported here. Finally, the electron heat flux (2.10) can be expressed using the Fourier amplitudes of the fluctuations as follows:

$$Q = \frac{3}{2} n_e T_e v_{\mathrm{the}} \sum_{\boldsymbol{k}} i k_y \rho_e \varphi^*_{\boldsymbol{k}} \frac{\delta T_{e,\boldsymbol{k}}}{T_e}. \tag{4.6}$$

Together, (4.1)–(4.3) and (4.5) form an asymptotic model derived in an electrostatic, collisional limit of GK in a straight and uniform magnetic field with $\hat{\boldsymbol{b}} = \hat{\boldsymbol{z}}$ (Adkins *et al.* 2023). They describe the electrostatic dynamics of fluctuations on perpendicular and parallel scales that satisfy

$$k_\parallel L_T \sim \sqrt{\sigma}, \quad k_\perp \rho_\perp \sim 1, \quad \rho_\perp \equiv \frac{\rho_e}{\sigma}\frac{L_T}{\lambda_{ei}}, \tag{4.7}$$

where $L_T^{-1} \equiv -\partial \ln T_e/\partial x$ is the electron-temperature gradient, λ_{ei} is the electron-ion mean free path and σ is a formal scaling parameter that is arbitrary provided it satisfies $\beta_e \ll \sigma \ll 1$. The fact that this parameter is arbitrary is a consequence of the scale invariance of the model (Adkins *et al.* 2023). This implies a particular scaling of the heat flux with the square of the normalised parallel system size, *viz*.

$$Q \propto \left(\frac{L_\parallel \sqrt{\sigma}}{L_T}\right)^2. \tag{4.8}$$

Similarly, any intrinsic time scales in (4.1)–(4.3) (e.g. the outer-scale injection rate γ^{o}) can be shown to be proportional to the inverse square of the normalised parallel box size. The numerical results for the (electron) heat flux Q and any relevant rate γ (e.g. γ_E, $\gamma_{\boldsymbol{k}}$, γ^{o}, etc.) can, therefore, be presented in terms of the following normalised quantities:

$$\hat{Q} \equiv \left(\frac{L_T}{L_\parallel \sqrt{\sigma}}\right)^2 \frac{Q}{(\rho_\perp/\rho_e) Q_{\mathrm{gB}e}}, \tag{4.9}$$

$$\hat{\gamma} \equiv \left(\frac{L_T}{L_\parallel \sqrt{\sigma}}\right)^{-2} \frac{\gamma}{\omega_\perp}, \tag{4.10}$$

where $Q_{\mathrm{gB}e} = n_e T_e v_{\mathrm{the}} (\rho_e/L_T)^2$ is the gyro-Bohm heat flux and

$$\omega_\perp = \rho_e v_{\mathrm{the}}/2\rho_\perp L_T \tag{4.11}$$

is the value of the electron drift frequency at $k_y\rho_\perp = 1$. A direct consequence of the scale invariance of (4.1)–(4.3) is that $\hat{Q}$ must be independent of L_T and the

https://doi.org/10.1017/S0022377825000054 Published online by Cambridge University Press

	$L_\perp/\rho_\perp$	$L_\parallel\sqrt{\sigma}/L_T$	$n_\perp$	$n_\parallel$	$\nu_\perp\rho_e^4/\omega_\perp\rho_\perp^4$	$\hat{\gamma}_{\max}$
Sim1	100	50	341	31	5×10^{-4}	6.3×10^{2}
Sim2	100	50	683	43	1×10^{-4}	1.1×10^{3}
Sim3	70	40	191	31	5×10^{-4}	4.1×10^{2}
Sim4	40	30	191	31	5×10^{-5}	4.9×10^{2}

TABLE 1. A summary of the simulation parameters used in § 4.1. The simulation domain is taken to be 'square' with $L_x = L_y = L_\perp$ and $n_x = n_y = n_\perp$, where n_x, n_y and $n_\parallel$ are the number of resolved (i.e. after dealiasing – see Appendix B) Fourier modes in the x, y and z coordinates, respectively. The last column shows the maximum growth rate $\gamma_{\max}$ normalised according to (4.10).

perpendicular box size (in any direction, provided L_x and L_y are sufficiently large); therefore, it is a function of $\hat{\gamma}_E$ only. Note that all of the aforementioned scalings are valid only when the hyperviscous cut-off is far from the outer scale, i.e. when $\nu_\perp$ is small enough and so does not upset the scale invariance of the outer-scale quantities.

In the absence of flow shear, the nonlinear saturated state of (4.1)–(4.3) has been investigated extensively and exhibits a critically balanced local energy cascade (Adkins *et al.* 2023). Therefore, (4.1)–(4.3) with $\gamma_E \neq 0$ should give rise to the kind of turbulence that is described by the theory laid out in § 3. Here, we show data from four sets of simulations where we varied γ_E while keeping all other parameters fixed, as detailed in table 1.

Figure 4(*a*) shows the dependence of $\hat{Q}$ on $\hat{\gamma}_E$ for these simulations. The agreement with figure 3 is evident. The predicted scaling of the heat flux in the weak-shear regime (3.20) holds very well up to $\hat{\gamma}_E \approx 100$. This is followed by a swift transition to the strong-shear scaling (3.27). Recall that the theory of § 3.2.1 predicts that the transition between the two regimes should occur at $\gamma_E \sim \gamma^{\mathrm{o}}(0)$, where the energy-injection rate at the outer scale $\gamma^{\mathrm{o}}(0)$ is approximately the linear-instability growth rate $\gamma_{\boldsymbol{k}}$ at the outer scale. Using the outer-scale estimates presented in figure 4(*b*), we find that $k_y^{\mathrm{o}}(0)\rho_\perp \approx 0.3$. Solving the linear dispersion relation for (4.1)–(4.3) for Sim1 at $k_x = 0$, $k_y\rho_\perp = 0.35$ and substituting $k_\parallel L_T/\sqrt{\sigma} = 2\pi/50$ for the box-sized mode in the parallel direction, we obtain an approximation of the normalised outer-scale injection rate of $\hat{\gamma}^{\mathrm{o}}(0) \sim \hat{\gamma}_{\boldsymbol{k}} \approx 70$, consistent with the numerically observed transition at $\hat{\gamma}_E \approx 100$.[9]

Figure 4(*b*) shows that $k_x^{\mathrm{o}}(\gamma_E)$ and $k_y^{\mathrm{o}}(\gamma_E)$ are consistent with the behaviour of the outer scale predicted in § 3.2. As γ_E is increased, k_y^{o} stays roughly constant until k_x^{o} catches up with it, whereafter the system transitions into the strong-shear regime where k_x^{o} and k_y^{o} remain comparable and both increase linearly with γ_E, as predicted in § 3.2.2. This behaviour persists until k_y^{o} reaches (approximately) the poloidal wavenumber at which the linear growth rate is maximal. For γ_E larger than $\gamma_{\max}$, the turbulence is completely suppressed. This behaviour is also visually

[9]Given the discussion in footnote 4, we must mention that this $k_\parallel$ maximises the growth rate at the given k_y. The reader might also wonder why we consider $k_x = 0$ given that the outer-scale radial wavenumber is not zero. Since k_x enters the linear dispersion relation only via the hyperviscous dissipation, the growth rate is virtually independent of k_x at these scales.

https://doi.org/10.1017/S0022377825000054 Published online by Cambridge University Press

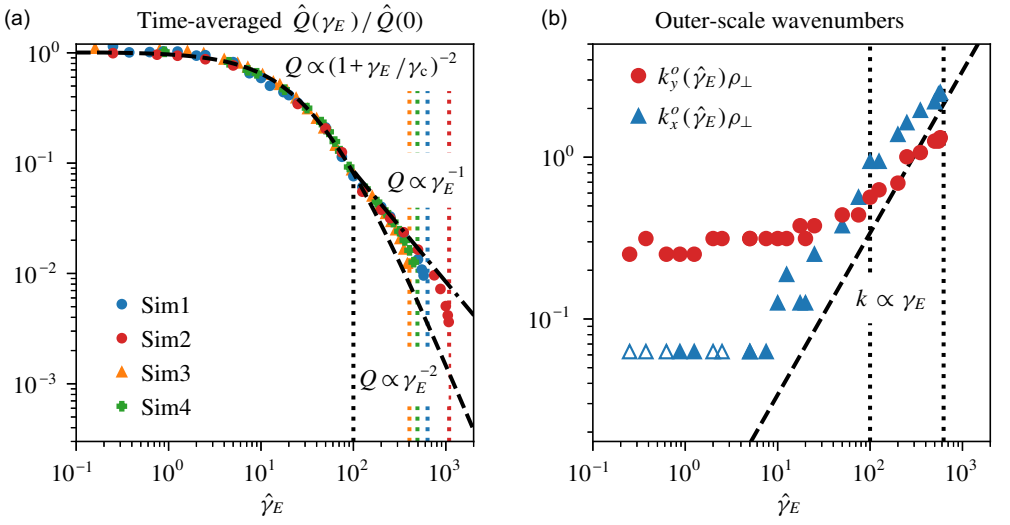


FIGURE 4. (*a*) Time-averaged, saturated radial turbulent heat flux, normalised to its value at zero flow shear, as a function of normalised flow shear $\hat{\gamma}_E$ [normalised per (4.10)] for the sets of simulations detailed in table 1. The data from all four sets overlay due to the scale invariance of (4.1)–(4.3). The black dashed and dash-dotted lines show the theoretical predictions (3.20) and (3.27), respectively, where, for the former, the curve is plotted using $\hat{\gamma}_c \approx 39$, found by fitting to the data presented here. The vertical black dotted line marks the approximate shearing rate $\hat{\gamma}_E \approx 100$ where the system transitions from the weak- to the strong-shear regime. The values of $\gamma_E \approx \gamma_{\max}$ are shown using vertical dotted lines of the same colour as the data points for each respective set of simulations. (*b*) Outer-scale wavenumbers $k_x^o(\gamma_E)$ and $k_y^o(\gamma_E)$, defined as those that maximise (4.12) and (4.13), respectively, for the Sim1 set of simulations. The dashed line indicates a linear dependence on the flow shear, $k \propto \gamma_E$. The left vertical dotted line is the same as in panel (*a*) and marks the location $\gamma_E \approx 100$ where the system transitions from the weak- to the strong-shear regime. In the former, k_y^o is (approximately) pinned to $k_y^o(0)$, but k_x^o increases linearly with γ_E. In the strong-shear regime, $k_x^o \sim k_y^o \propto \gamma_E$. The right vertical dotted line indicates the value of flow shear that is equal to the largest growth rate $\gamma_{\max}$, where the outer scale k_y^o reaches, at least approximately, the scale of the most unstable mode $k_{y,\max}\rho_\perp \approx 3.7$. Note that, at low γ_E, (4.12) is sometimes maximised at $k_x = 0$. In those cases, represented by the hollow triangles, we have set $k_x^o\rho_\perp$ to the box scale $2\pi\rho_\perp/L_x \approx 0.063$.

confirmed by figure 5, where we show real-space snapshots from simulations with different flow shear.

The outer-scale wavenumbers shown in figure 4 are defined as those that maximise the (steady-state) poloidally and radially averaged heat fluxes, defined respectively as

$$\langle Q\rangle_y(k_x) \equiv \frac{3}{2} n_e T_e v_{the} \sum_{k_y,k_\parallel} ik_y \rho_e \varphi_{\boldsymbol{k}}^* \frac{\delta T_{e,\boldsymbol{k}}}{T_e}, \tag{4.12}$$

$$\langle Q\rangle_x(k_y) \equiv \frac{3}{2} n_e T_e v_{the} \sum_{k_x,k_\parallel} ik_y \rho_e \varphi_{\boldsymbol{k}}^* \frac{\delta T_{e,\boldsymbol{k}}}{T_e}, \tag{4.13}$$

where $\varphi_{\boldsymbol{k}}$ and $\delta T_{e,\boldsymbol{k}}$ are the three-dimensional Fourier amplitudes of the fields. The ratio of the heat flux at the transition to that at zero flow shear is found to be

https://doi.org/10.1017/S0022377825000054 Published online by Cambridge University Press

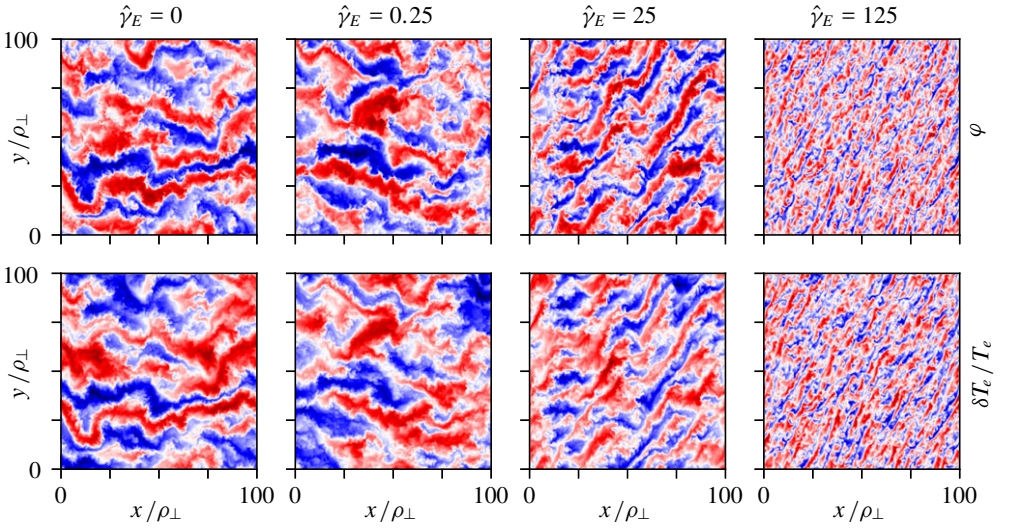


FIGURE 5. Snapshots of φ (top row) and $\delta T_e/T_e$ (bottom row) in the (x, y) plane for Sim1 simulations with four different values of γ_E, as specified above each column. For each snapshot, the amplitudes are normalised to lie in the range $[-1, 1]$, with the values in this interval corresponding to colours between dark blue and dark red, respectively. The second column corresponds to the weak-shear regime (i) from figure 3(*a*), where the flow shear is too weak to influence the saturated state significantly. The third column also corresponds to the weak-shear regime, with $k_y^{\mathrm{o}}(\gamma_E)$ pinned to $k_y^{\mathrm{o}}(0)$ but with $k_x^{\mathrm{o}}(\gamma_E)$ increased by the influence of the flow shear, which here clearly manifests itself as the tilting of the eddies. In this case, the structures have a similar size in y to those in the first- and second-row panels, but a shorter length scale in x due to being sheared. The last column shows the saturated state in the strong-shear regime (ii) of figure 3(*a*), where the flow shear has manifestly pushed the outer scale to much shorter wavelengths.

approximately $Q(0)/Q(\hat{\gamma}_E = 100) \approx 13$, which, according to (3.20), would require $\mathcal{A}^{\mathrm{o}}(0) \approx 0.4$, consistent with $k_x^{\mathrm{o}}/k_y^{\mathrm{o}} \approx 0.3$, as seen in figure 4 at low values of flow shear. Given the remarkably good fit for Q as a function of γ_E, the small discrepancy is likely due to our estimates of k_x^{o} and k_y^{o} via (4.12) and (4.13) being an imperfect measure of the outer scale. For instance, (4.12) fails to produce a nonzero estimate for k_x if γ_E is too low or zero. Note that the scale invariance of the fluid system implies that the streamer aspect ratio $\mathcal{A}^{\mathrm{o}}(0)$ of (4.1)–(4.3) is not a function of any of the parameters of the system; i.e. it is just an order-unity (albeit measurably, and consequentially, smaller than unity) constant, so it is not possible to perform a scan in $\mathcal{A}^{\mathrm{o}}(0)$.

For values of γ_E comparable to, or larger than, the maximum growth rate $\gamma_{\max}$, the turbulence is strongly suppressed, as expected. However, this occurs in a surprising and nontrivial way – turbulence becomes radially localised into disjoint turbulent patches (see figure 6). This localisation is reminiscent of the formation of coherent structures called 'ferdinons' in sheared ITG turbulence (van Wyk *et al.* 2016, 2017; Ivanov *et al.* 2020). Despite their qualitative similarities, the localised ETG structures reported here differ in a number of ways from the ITG ferdinons observed in similar fluid simulations by Ivanov *et al.* (2020): the former are three-dimensional structures (i.e. require a nonzero $k_\parallel$) that drift radially in the absence of magnetic drifts, while the latter exist in two dimensions and depend on the poloidal magnetic drift for their

https://doi.org/10.1017/S0022377825000054 Published online by Cambridge University Press

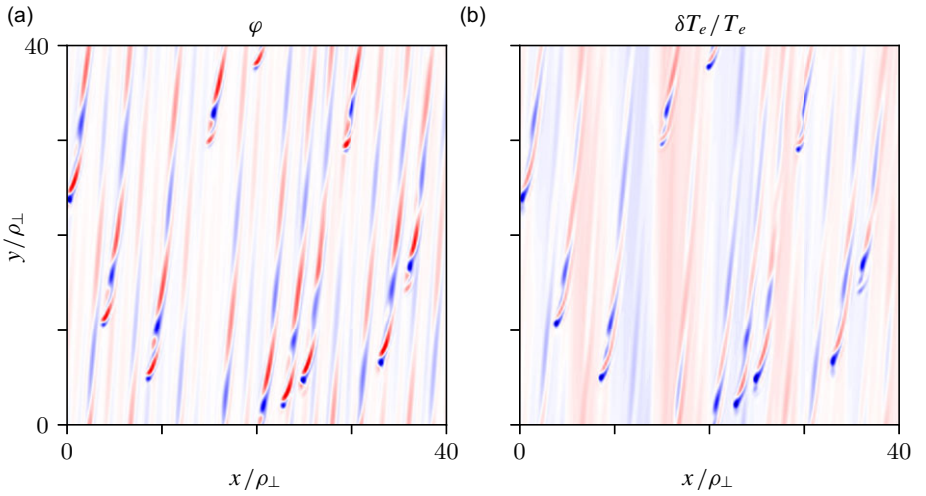


FIGURE 6. Radial localisation of turbulent perturbations at very large values of flow shear. Taken from a Sim4 simulation with $\hat{\gamma}_E = 540$, which is just over the largest growth rate $\hat{\gamma}_{\max} \approx 493$. The simulation has achieved a steady state with time-averaged normalised heat flux $\hat{Q}(\gamma_E)/\hat{Q}(0) \approx 4 \times 10^{-7}$, which is why it is not visible in figure 4.

radial motion. The radial localisation of sheared turbulence through the formation of coherent structures appears to be a universal phenomenon, whose detailed investigation is the subject of our ongoing work that falls outside the scope of this paper. Here, we note that, apart from the poloidally localised structures shown in figure 6 and reported by van Wyk *et al.* (2016) and Ivanov *et al.* (2020), solitary travelling structures that are localised only radially and consist of a single poloidal harmonic (i.e. a single k_y) have been seen in various models of sheared plasma turbulence (Pringle, Mcmillan & Teaca 2017; McMillan *et al.* 2009, 2018; Zhou *et al.* 2019, 2020). We find no such structures and it remains an open question exactly what is the determining factor for their appearance.

4.2. *Gyrokinetic ITG turbulence*

We now explore the validity of our theory for plasma turbulence in axisymmetric toroidal geometry. Using the GK code GENE, we performed numerical flux-tube simulations of ITG-driven turbulence with modified adiabatic electrons (Hammett *et al.* 1993) in a Cyclone-base-case (CBC) (Lin *et al.* 1999; Dimits *et al.* 2000) geometry with normalised magnetic shear $\hat{s} = 0.796$, safety factor $q = 1.4$ and inverse aspect ratio $\epsilon = 0.18$. We focus on two values of the ion-temperature gradient, $R/L_{T_i} = 10$ and $R/L_{T_i} = 14$, box sizes corresponding to the smallest wavenumbers $k_{x,\min}\rho_i = 1.6 \times 10^{-2}$ and $k_{y,\min}\rho_i = 6.25 \times 10^{-3}$, $n_x = 288$ radial modes, $n_y = 256$ poloidal modes for $R/L_{T_i} = 10$ and $n_y = 512$ for $R/L_{T_i} = 14$, $n_z = 16$ parallel grid points, and velocity-space resolution $n_v = 32$ (parallel velocity), $n_\mu = 8$ (magnetic moment). We performed scans of the equilibrium perpendicular flow shear γ_E, with parallel flow shear turned off. Note that the temperature gradients that we consider are significantly above the nominal CBC value of $R/L_{T_i} = 6.92$. This is done to

https://doi.org/10.1017/S0022377825000054 Published online by Cambridge University Press

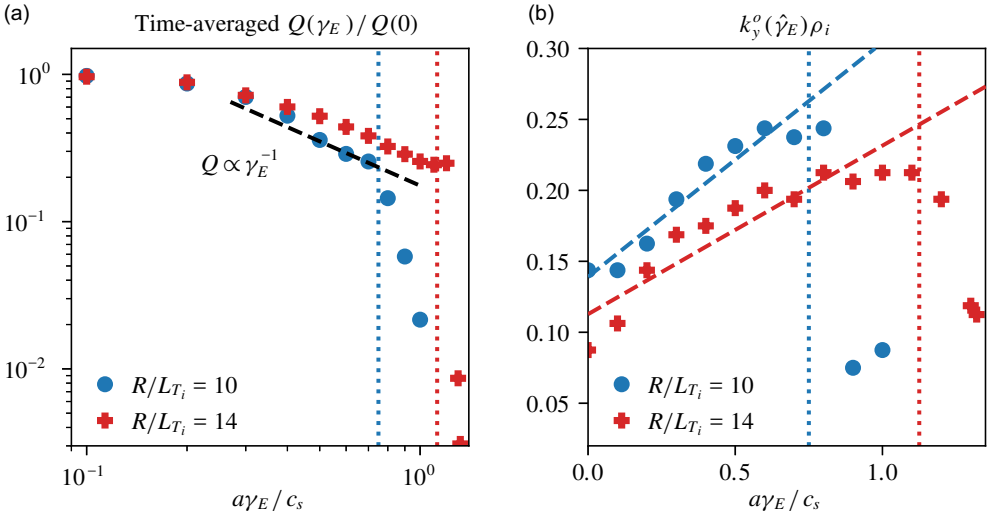


FIGURE 7. (*a*) Time-averaged, saturated-state, radial turbulent heat flux, normalised to its value at $\gamma_E = 0$ and (*b*) outer-scale poloidal wavenumber $k_y^o \rho_i$ as a function of the flow shear for two different values of the ion-temperature gradient (see § 4.2 for other relevant numerical parameters). The black dashed line corresponds to the trend $Q \propto \gamma_E^{-1}$, while the blue and red dashed lines are linear fits for k_y^o as a function of γ_E for each temperature gradient. The vertical dotted lines correspond to $1.5\gamma_{\max}$ for each of the simulations. The flow shear is normalised to a/c_s, where a is the minor radius and c_s is the ion sound speed.

ensure that the system is strongly driven and far from any marginal states where other physics, e.g. zonal flows, could be setting the saturated fluctuation levels.[10]

Figure 7 shows the dependence of the heat flux and poloidal outer-scale wavenumber on the shearing rate. The strong-shear scaling $Q \propto \gamma_E^{-1}$ (3.27) is followed reasonably well for both values of the ion-temperature gradient. Also, the dependence of k_y^o on γ_E is approximately linear, as expected from (3.26). Note that (3.26) is only an asymptotic scaling and for γ_E close to $\gamma^o(0)$, we have $k_y^o(\gamma_E) - k_y^o(0) \propto \gamma_E$. To calculate k_y^o for figure 7(*b*), we used the GK equivalent of (4.13), i.e. we approximated k_y^o by the k_y that has the largest contribution to the heat flux.

According to the theory presented in § 3.2.2, the strong-shear regime should end at $\gamma_E \sim \gamma_{\max}$. Indeed, for both values of R/L_{T_i}, the $Q \propto \gamma_E^{-1}$ dependence lasts roughly up to $\gamma_E/\gamma_{\max} \approx 1.5$, after which the heat flux is sharply suppressed. Note the absence of the weak-shear scaling (3.20) – this is expected because the unsheared ($\gamma_E = 0$) ITG turbulence in this case has $\mathcal{A}^o(0) \sim 1$. Consequently, the heat flux is (approximately) constant in the weak-shear regime and the dependence of Q on γ_E resembles figure 3(*b*).

[10]Indeed, the assumption that saturation at the outer scale is determined by a balance between linear and nonlinear rates (see § 3.1) is likely incorrect for ion-scale turbulence below the Dimits threshold (Dimits *et al.* 2000), where the fluctuations are regulated by strong long-lived zonal flows (Rogers *et al.* 2000; Diamond *et al.* 2005; Zhu *et al.* 2020*a*,b; Ivanov *et al.* 2020). Investigating the influence of equilibrium flow shear on the Dimits state is outside of the scope of this paper.

https://doi.org/10.1017/S0022377825000054 Published online by Cambridge University Press

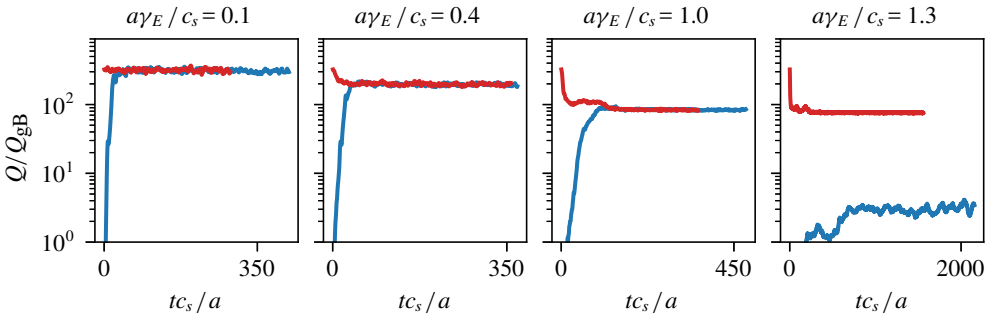


FIGURE 8. Radial turbulent heat flux versus time for $R/L_{T_i} = 14$ and four different values of γ_E, as labelled in the title of each panel. The blue lines are time traces from simulations initialised with small-amplitude noise, while the red ones represent simulations restarted from a saturated $\gamma_E = 0$ run.

4.2.1. Bistability of high-shear states

At large values of flow shear $\gamma_E > \gamma_{\max}$, i.e. beyond the strong-shear regime, we find that the system can saturate at (at least) two different levels of heat transport. Figure 8 shows the time traces of the turbulent heat flux for $R/L_{T_i} = 14$ and four different values of γ_E, where, for each value of the flow shear, the simulations were initialised either with small-amplitude noise or with data from a saturated $\gamma_E = 0$ simulation. For $a\gamma_E/c_s \leqslant 1$, the saturated state is found to be independent of the initial conditions. In contrast, a simulation with $a\gamma_E/c_s = 1.3$ initialised with a small-amplitude noise (corresponding to the rightmost point in figure 7) saturates with a time-averaged radial heat flux that is nearly two orders of magnitude smaller than that obtained by restarting it from an already saturated high-amplitude state. Similar bistability in gyrokinetic turbulence with mean flow shear has been reported by Christen *et al.* (2022). The physics of this phenomenon, as observed in the simulations presented in figure 8, falls outside of the range of validity of the theory presented in § 3 because, at least in the case investigated here, it happens only at $\gamma_E > \gamma_{\max}$, where the assumption of a balance between the rates of shearing and energy injection (3.25) is not expected to hold.

Finally, we note that the appearance of coherent structures (whether of the poloidally localised kind or not, see the discussion at the end of § 4.1) can naturally lead to nonunique saturation. Indeed, if the saturated state is a collection of localised structures, then volume-averaged turbulent quantities, like the heat flux, are proportional to the number of structures in the simulation domain (van Wyk *et al.* 2016). If these structures happen to be well localised and noninteracting (or only weakly interacting), then their number in the simulation domain is not necessarily uniquely determined, but can be a function of the initial conditions and/or of the perpendicular box size. The turbulent fluctuations in the low-transport saturated state displayed in figure 9 show signs of spatial localisation (as opposed to those in the high-transport state), even if not quite as obviously as they do in the ETG turbulence shown in figure 6.

5. Momentum transport

We have thus far focused on the influence of imposed flow shear on the turbulent heat transport. In sheared systems, another important quantity of interest is the

https://doi.org/10.1017/S0022377825000054 Published online by Cambridge University Press

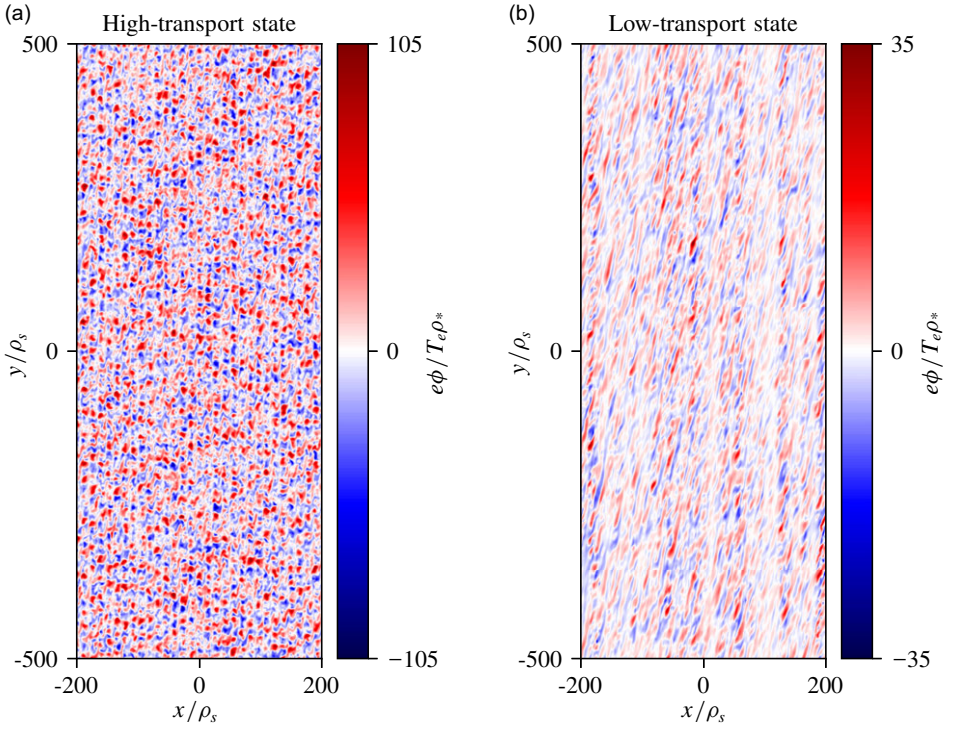


FIGURE 9. Snapshots of the electrostatic potential in the perpendicular plane from the (*a*) saturated high-transport and (*b*) low-transport states with $R/L_{T_i} = 14$ and $a\gamma_E/c_s = 1.3$, whose heat-flux time traces are shown in blue and red, respectively, in the bottom right panel of figure 8. The perpendicular coordinates are normalised to the ion sound radius ρ_s. Note that the aspect ratio of the panels corresponds to that of the simulation domain.

turbulent transport of momentum, which is crucial for driving and maintaining equilibrium differential rotation in fusion experiments. Such rotation is typically achieved using neutral beams that deposit both energy and momentum into the plasma. The profiles of temperature and equilibrium flow are then determined by the turbulent heat diffusivity and turbulent viscosity, which are usually larger than their collisional counterparts. The simplifying choice of a purely perpendicular flow made in § 3.2 means that we are unable to describe all of the relevant physics: e.g. we are missing the effect of the parallel-velocity-gradient instability, which can be the main driver of transport at high γ_E (Highcock *et al.* 2010; Barnes *et al.* 2011).[5] Nevertheless, the theory derived in § 3.2 makes numerically falsifiable predictions for the momentum transport of turbulence with imposed flow shear. Let us investigate them here.

Consider the fluid ETG model described in § 4.1, wherein we have imposed a mean flow in the poloidal y direction that varies along the radial x direction. This flow then allows the plasma to have nonzero radial transport of poloidal momentum, defined, similarly to (2.10), as

$$\Pi \equiv \sum_s m_s \int \frac{\mathrm{d}^3\boldsymbol{r}}{V} \int \mathrm{d}^3\boldsymbol{w}\, (\boldsymbol{v}_E \cdot \nabla x)(\boldsymbol{w} \cdot \nabla y)\delta f_s. \tag{5.1}$$

https://doi.org/10.1017/S0022377825000054 Published online by Cambridge University Press

It can be shown (see Appendix C) that, in the fluid model described in § 4.1, (5.1) becomes

$$\Pi = -\frac{n_e T_e \rho_e^2}{2} \int \frac{\mathrm{d}^3 \boldsymbol{r}}{V} \frac{\partial \varphi}{\partial y} \frac{\partial}{\partial x} \left[\left(1 + \frac{Z T_e}{T_i} \right) \varphi - \frac{\delta T_e}{T_e} \right]. \tag{5.2}$$

As expected, Π is written as the sum of the Reynolds stress of the $\boldsymbol{E} \times \boldsymbol{B}$ flow and a diamagnetic stress (Smolyakov, Diamond & Medvedev 2000; Ivanov *et al.* 2020; Sarazin *et al.* 2021). Note that Π itself is of no relevance to the dynamics of the fluctuations as it does not enter (4.1)–(4.3) at all, unlike Q, which is responsible for the injection of energy, as per (2.7).

Just like we did for the heat flux Q in § 3.1.1, we can estimate Π as

$$\Pi \sim n_e T_e k^{\mathrm{o}}_{x,\mathrm{tilt}} k^{\mathrm{o}}_y \rho_e^2 (\overline{\varphi}^{\mathrm{o}})^2, \tag{5.3}$$

where

$$k^{\mathrm{o}}_{x,\mathrm{tilt}}(\gamma_E) \equiv k^{\mathrm{o}}_x(\gamma_E) - k^{\mathrm{o}}_x(0) \sim k^{\mathrm{o}}_y(\gamma_E) \tau^{\mathrm{o}}_{\mathrm{nl}}(\gamma_E) \gamma_E. \tag{5.4}$$

Using $k^{\mathrm{o}}_{x,\mathrm{tilt}}$ instead of k^{o}_x in (5.3) is necessary because, in the absence of flow shear, the GK equation (2.1) obeys the symmetry

$$(x, y, z) \mapsto (-x, y, -z), \quad w_\parallel \mapsto -w_\parallel, \quad \phi \mapsto -\phi, \quad h_s \mapsto -h_s, \tag{5.5}$$

under which $\Pi \mapsto -\Pi$ and so the time-averaged Π must vanish if $\gamma_E = 0$ (Parra *et al.* 2011b; Sugama *et al.* 2011; Fox *et al.* 2017). Thus, only the part of k_x associated with the eddy tilting contributes to the momentum flux.[11]

Using (3.2) and (3.6), we write (5.3) as

$$\frac{\Pi}{n_e T_e} \sim \frac{\gamma_E \gamma^{\mathrm{o}}}{\Omega_e^2} \frac{1}{(k^{\mathrm{o}}_x \rho_e)^2} \sim \frac{\gamma_E \gamma^{\mathrm{o}}}{\Omega_e^2} \frac{1}{(\mathcal{A}^{\mathrm{o}} k^{\mathrm{o}}_y \rho_e)^2}. \tag{5.6}$$

In the weak-shear regime (§ 3.2.1), where $\gamma_E < \gamma^{\mathrm{o}}(0)$, the linear and nonlinear times at the outer scale are given by (3.15), and the fluctuation aspect ratio at the outer scale satisfies (3.18), we find

$$\frac{\Pi(\gamma_E)}{\Pi(0)} \propto \frac{\gamma_E}{(1 + \gamma_E/\gamma_{\mathrm{c}})^2}. \tag{5.7}$$

Note that if $\mathcal{A}^{\mathrm{o}}(0) \sim 1$, i.e. if the turbulence is isotropic in the absence of flow shear, then $\gamma_{\mathrm{c}} \sim \gamma^{\mathrm{o}}(0)$ and Π is (approximately) proportional to γ_E in the weak-shear regime, unlike Q, which would be constant in this case (see figure 3*b*). In the

[11] A careful reader may spot another issue, which is also resolved by using $k_{x,\mathrm{tilt}}$ instead of k_x. Recall the discussion after (3.7), where we justified estimating Q via its value at the outer scale by arguing that the contributions from smaller scales decay with increasing k_y. If we were to estimate naïvely the contribution $\overline{\Pi}(k_y)$ to Π from scale k_y in the inertial range as $\overline{\Pi}(k_y) \propto k_x k_y \overline{\varphi}^2$, the inertial-range spectrum (3.5) would imply $\overline{\Pi}(k_y) \propto k_y^{2/3}$, leading one to believe that the integral (5.1) is dominated by the small-scale end of the inertial range rather than by the outer scale. This argument is, however, incorrect. In the inertial range, as k_y increases, the nonlinear time decreases according to (3.5), limiting the effect of the flow shear and thus decreasing $\overline{\Pi}(k_y)$. To capture this, the correct estimate is $\overline{\Pi}(k_y) \propto k_{x,\mathrm{tilt}} k_y \overline{\varphi}^2$, where $k_{x,tilt} \sim k_y \tau_{\mathrm{nl}} \gamma_E \propto k_y^{-1/3}$ in the inertial range. This then leads to $\overline{\Pi}(k_y) \propto k_y^{-2/3}$ and so Π is dominated by the contributions are the outer scale.

https://doi.org/10.1017/S0022377825000054 Published online by Cambridge University Press

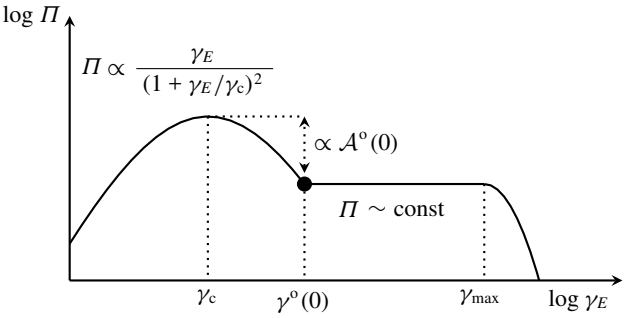


FIGURE 10. A qualitative diagram of the momentum flux Π versus flow shear γ_E in the fluid ETG model (see figure 4 for a similar diagram for the heat flux Q). The indicated ratio between the plateau in the strong-shear regime and the peak of Π at $\gamma_E = \gamma_c$ formally holds when $\mathcal{A}^o(0) \ll 1$.

strong-shear regime (§ 3.2.2), where $\gamma_E > \gamma^o(0)$, the fluctuations satisfy $\mathcal{A}^o(\gamma_E) \sim 1$, and (3.25) and (3.26) hold, we find

$$\Pi(\gamma_E) \propto \gamma_E^0, \tag{5.8}$$

i.e. the momentum flux is independent of the imposed flow shear (see figure 10). Crucially, in both regimes,

$$\frac{\Pi}{Q} \propto \gamma_E. \tag{5.9}$$

This can also be seen directly from (3.8) and (5.6), which imply

$$\frac{\Pi v_{the}}{Q} \sim \frac{\gamma_E}{\gamma^o} k_y^o \rho_e, \tag{5.10}$$

and so (5.9) follows immediately if $\gamma^o \propto k_y^o$, as we have assumed throughout § 3.2. If we define the normalised turbulent viscosity ν and diffusivity χ as

$$\nu \equiv \frac{\Pi}{n_e m_e \gamma_E}, \quad \chi \equiv \frac{Q}{n_e T_e L_T^{-1}}, \tag{5.11}$$

then the turbulent Prandtl number is

$$\mathrm{Pr} = \frac{\nu}{\chi} = \frac{\Pi}{Q} \frac{v_{the}^2}{2\gamma_E L_T}. \tag{5.12}$$

According to (5.9), this is independent of γ_E. This prediction is consistent with previous GK studies of turbulent transport in sheared turbulence (Highcock *et al.* 2010; Barnes *et al.* 2011).

Figure 11(*a*) shows the values of turbulent heat and momentum flux from the Sim1 and Sim2 sets of simulations, detailed in table 1. There is good agreement with the weak-shear scaling (5.7). According to (5.7), Π should peak in the weak-shear regime at $\gamma_E = \gamma_c = \mathcal{A}^o(0)\gamma^o(0)$. For the Sim1 and Sim2 simulations, whose data are presented in figure 11, the transition to the strong-shear regime happens

https://doi.org/10.1017/S0022377825000054 Published online by Cambridge University Press

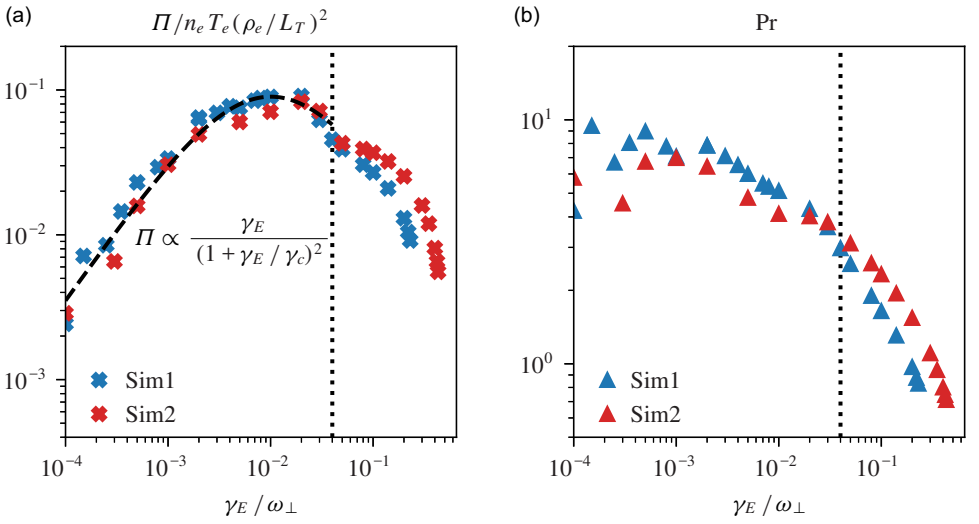


FIGURE 11. (*a*) Radial flux of poloidal momentum in the fluid ETG model (5.2) as a function of γ_E from simulation sets Sim1 and Sim2 (see table 1). The black dashed line is the best-fit line of the form (5.7) to the data up to $\gamma_E/\omega_\perp = 0.04$ (denoted by the vertical dotted line), where the system transitions from the weak- to the strong-shear regime (see also figure 4). (*b*) Prandtl number, defined as (5.12) for the same simulations as in panel (*a*).

at $\gamma^{\mathrm{o}}(0)/\omega_\perp \approx 0.04$, where $\omega_\perp$ is given by (4.11) (see also figure 4). As discussed in § 4.1, we find that, numerically, $\mathcal{A}^{\mathrm{o}}(0) \approx 0.4$, which gives $\gamma_{\mathrm{c}}/\omega_\perp \approx 0.016$, consistent with the observed peak in Π at $\gamma_E/\omega_\perp \approx 0.01$. However, the prediction that Π should be constant in the strong-shear regime is not observed, likely due to finite-hyperviscosity effects and the finite extent of the inertial range. Our theory does not take into account the finite value of hyperviscosity necessary to achieve a saturated state numerically. Since Π is a higher-order Fourier-space moment of the fluctuation spectrum than Q, it is more sensitive to the spectrum at high k, where hyperviscous effects matter. These effects become more important as γ_E increases and the inertial range shortens (see also figure 12 in Appendix A). As figure 11(*a*) shows, the simulations with lower hyperviscosity (Sim2) have a weaker dependence of Π on γ_E in the strong-shear regime, consistent with the hypothesis that the hyperviscous cut-off is responsible for the discrepancy with the theoretical prediction (5.8). Figure 11(*b*) shows that the numerically measured Prandtl number is weakly dependent on γ_E, varying only by approximately a factor of two over a range for γ_E of nearly three orders of magnitude, before decreasing at large γ_E where hyperviscous effects become important.

The nonmonotonic weak-shear dependence (5.7), which has a local maximum at $\gamma_E = \gamma_{\mathrm{c}}$, implies that, for the same value of Π, two distinct values of γ_E, and so of Q, are possible. This suggests that sheared anisotropic turbulence may be prone to transport bifurcations similar to those discussed by Highcock *et al.* (2010, 2011) and Parra *et al.* (2011a). Of course, our oversimplified model of electron-scale turbulence cannot be applied directly to any experimental studies. Nevertheless, our theory suggests that if experimentally relevant turbulence is dominated by streamers, transport bifurcations might exist.

https://doi.org/10.1017/S0022377825000054 Published online by Cambridge University Press

6. Summary and discussion

Starting from the standard picture of turbulent saturation via a local energy cascade (§ 3.1), we have developed a theory for the effect of mean perpendicular flow shear on temperature-gradient-driven turbulence in fusion plasmas. As argued in § 3.2, it is meaningful to distinguish two different regimes depending on the ratio of the shearing rate γ_E to the rate $\gamma^{\mathrm{o}}(0)$ of energy injection in the corresponding system with zero flow shear.

In the weak-shear regime, defined by $\gamma_E < \gamma^{\mathrm{o}}(0)$, the poloidal outer scale and the energy-injection rate remain approximately the same as when $\gamma_E = 0$, but the radial outer scale decreases with increasing γ_E (3.18) due to the tilting of turbulent eddies by the shear. The extent to which the flow shear is able to suppress the turbulent transport in this regime is linked to the aspect ratio of the outer-scale fluctuations at zero flow shear, $\mathcal{A}^{\mathrm{o}}(0) = k_x^{\mathrm{o}}(0)/k_y^{\mathrm{o}}(0)$. We find that turbulence with $\mathcal{A}^{\mathrm{o}}(0) \sim 1$ is largely unaffected by flow shear unless the shear is comparable to, or larger than, $\gamma^{\mathrm{o}}(0)$. In contrast, heat transport in streamer-dominated turbulence with $\mathcal{A}^{\mathrm{o}}(0) \ll 1$, which is often encountered in fusion-relevant contexts, is shown to be strongly suppressed by flow shear even at $\gamma_E \ll \gamma^{\mathrm{o}}(0)$ as long as $\gamma_E \gtrsim \gamma_{\mathrm{c}}$, where the critical shearing rate γ_{c} (3.19) is smaller than $\gamma^{\mathrm{o}}(0)$ by a factor of $\mathcal{A}^{\mathrm{o}}(0)$. This reflects the intuitive notion that radially elongated fluctuations should be more susceptible to sheared poloidal flows.

At $\gamma_E > \gamma^{\mathrm{o}}(0)$, the system is in the strong-shear regime, where the outer scale is determined by the balance among the shearing, energy-injection and nonlinear mixing rates (3.25), and the outer-scale perpendicular wavenumbers grows proportionally to γ_E. Turbulence in the strong-shear regime is found always to have $k_x^{\mathrm{o}} \sim k_y^{\mathrm{o}}$, even if it was dominated by streamers at $\gamma_E = 0$. This is due to the shear-induced tilting of the turbulent fluctuations, which forces them to have $\mathcal{A}^{\mathrm{o}}(\gamma_E) \sim 1$ in this regime.

Our theoretical predictions for the dependence of the radial turbulent heat flux on the rate of perpendicular flow shear, (3.20) and (3.27), are confirmed to hold over a range of four orders of magnitude for the flow shear in idealised fluid ETG simulations (§ 4.1). Additionally, GK flux-tube simulations of ITG turbulence have demonstrated that our theory applies to more realistic models of plasma turbulence as well (§ 4.2). These two models are paradigmatic cases of turbulence with $\mathcal{A}^{\mathrm{o}}(0) \ll 1$ and $\mathcal{A}^{\mathrm{o}}(0) \sim 1$, respectively.

In addition to the heat-flux scalings, in § 5, we use our theory to predict the dependence of momentum flux on flow shear in the fluid ETG simulations. While not directly applicable to more realistic numerical simulations due to the restriction of purely perpendicular flow shear, our results suggest that streamer-dominated turbulent transport might exhibit transport bifurcations.

There exists a body of work on the suppression of turbulence by flow shear that is based on 'decorrelation theories' (Shaing, Crume & Houlberg 1990; Biglari, Diamond & Terry 1990; Zhang & Mahajan 1992, 1993; Hatch *et al.* 2018) stemming from Dupree (1972) or the equivalent derivation by Zhang & Mahajan (1993). There are some parallels that can be drawn between these theories and our approach: e.g. the definition of the normalised flow shear W by Zhang & Mahajan (1992) and Hatch *et al.* (2018) includes the crucial influence of the fluctuation aspect ratio and can be mapped to $\gamma_E/\mathcal{A}^{\mathrm{o}}(\gamma_E)\gamma^{\mathrm{o}}(0)$ in our notation. However, the derivation of our theory, as presented in § 3.2, is not related to these decorrelation theories and produces different scalings for the dependence of the heat flux on γ_E. For example, the

https://doi.org/10.1017/S0022377825000054 Published online by Cambridge University Press

functional dependence (3.20), borne out by the numerical results presented in § 4.1, is not reproduced by these theories. While the decorrelation theory by Zhang & Mahajan (1992) has been claimed to be applicable to some GK simulations (Hatch *et al.* 2018), we are (at this stage) unable to draw any conclusions about the more general applicability either of decorrelation theories or of the theory presented in § 3.2.

One possible application of the theory of sheared streamer-dominated turbulence described in § 3.2.1 is in the description of multiscale interactions in magnetised-plasma turbulence. Gyrokinetic theory and numerical analysis point to the existence of linear instabilities and turbulent fluctuations at two disparate perpendicular scales, *viz*. the gyroradii of the main ion species ρ_i and of the electrons ρ_e, often referred to as the 'ion' and 'electron' (perpendicular) scales, respectively. By virtue of the difference in the ion and electron masses, these two scales are well separated, *viz*. $\rho_e/\rho_i \sim \sqrt{m_e/m_i} \ll 1$. Furthermore, the GK ordering implies that the growth rate of electron-scale instabilities satisfies $\gamma_e \sim v_{\mathrm{th}e}/L$, while that of the ion-scale instabilities is $\gamma_i \sim v_{\mathrm{th}i}/L$, where L is some appropriate measure of the size of the device. Therefore, the fluctuations at these two spatial scales also occur on well-separated time scales: $\gamma_i/\gamma_e \sim \sqrt{m_e/m_i} \ll 1$. Nevertheless, numerically expensive GK simulations with enough resolution to span both ion and electron scales have shown that ion-scale turbulence can suppress electron-scale fluctuations (Candy *et al.* 2007; Waltz, Candy & Fahey 2007; Maeyama *et al.* 2015; Howard *et al.*, 2016*a*) and experimental results in support of this hypothesis have been reported (Howard *et al.* 2016*b*).

One possible mechanism for this suppression is that the turbulent ion-scale $\boldsymbol{E}\times\boldsymbol{B}$ flows shear away the electron-scale perturbations. However, if we assume that the electron-scale fluctuations satisfy $\mathcal{A}_e \sim 1$, this could not happen: the time scale associated with the ion-scale $\boldsymbol{E}\times\boldsymbol{B}$ shear is γ_i, while the growth rate of the electron-scale instabilities is $\gamma_e \gg \gamma_i$, so, by the quench rule, γ_i is too small to suppress the electron-scale turbulence.[12]

The theory of weakly sheared turbulence proposed in § 3.2.1 offers a possible alternative explanation. Simulations of electron-scale turbulence indicate that turbulence at those scales is dominated by radially elongated streamers, and, according to our theory, the ion-scale $\boldsymbol{E}\times\boldsymbol{B}$ shear will be relevant for shearing these streamers if they have $\mathcal{A}_e \ll 1$. In particular, if $k_{y,e}\rho_e \sim 1$ but $k_{x,e}\rho_i \sim 1$, i.e. if the ETG streamers have a radial size comparable to the scale of ion fluctuations, then the critical shear rate $\gamma_{\mathrm{c},e}$ for ETG turbulence (3.19) would be of the order of the ion-scale fluctuating $\boldsymbol{E}\times\boldsymbol{B}$ shear. Such an ordering would put the ion-scale shearing rate in the weak-shear regime for the ETG streamers, where (3.20) holds, with γ_E now representing the value of the flow shear that electron-scale fluctuations experience from the ion-scale ones. Therefore, the influence of this flow shear would be non-negligible, despite the naïve argument that might lead one to presume otherwise. Numerical experiments have indeed shown that the inclusion of ion-scale zonal flows (flux-surface-constant, poloidal $\boldsymbol{E}\times\boldsymbol{B}$ shear flows) in ETG simulations can drastically reduce the levels of electron-scale turbulence and transport, even though the ion-scale zonal-flow shear is much smaller than the growth rate of electron-scale

[12]Note that there are other mechanisms that could be responsible for such suppression, e.g. the parallel variation of the ion-scale $\boldsymbol{E}\times\boldsymbol{B}$ flow (Hardman *et al.* 2019, 2020), or ITG turbulence giving rise to shearing flows of small enough radial scale to influence the ETG eddies (Holland & Diamond 2004).

https://doi.org/10.1017/S0022377825000054 Published online by Cambridge University Press

instabilities (Waltz *et al.* 2007). Whether this mechanism for ITG suppression of electron-scale fluctuations is indeed realised in multiscale plasma turbulence appears to be a promising subject for future work.

Acknowledgements

We thank M. R. Hardman and F. I. Parra for inspiring discussions and invaluable feedback. We would also like to thank the organisers of the 14th Plasma Kinetics Working Meeting (2023) and its hosts at the Wolfgang Pauli Institute in Vienna, where a significant part of this work was first presented and discussed.

Editor Steve Tobias thanks the referees for their advice in evaluating this article.

Funding

This work was supported by the Engineering and Physical Sciences Research Council (EPSRC) [EP/R034737/1 and EP/W006839/1]. The work of A.A.S. was supported in part by the Simons Foundation via a Simons Investigator award. T.A. acknowledges the support of the Royal Society Te Apārangi, through Marsden-Fund grant MFP-UOO2221. Simulations were performed using resources provided by the Cambridge Service for Data Driven Discovery (CSD3) operated by the University of Cambridge Research Computing Service (www.csd3.cam.ac.uk), provided by Dell EMC and Intel using Tier-2 funding from the Engineering and Physical Sciences Research Council (capital grant EP/T022159/1), and DiRAC funding from the Science and Technology Facilities Council (www.dirac.ac.uk). To obtain further information on the data and models underlying this paper contact PublicationsManager@ukaea.uk.

Declaration of interests

The authors report no conflict of interest.

Appendix A. Isotropisation of streamer-dominated turbulence in the inertial range

Here, we develop the theory of the transition range between a streamer-dominated outer scale with $\mathcal{A}^{\mathrm{o}} \ll 1$ and an inertial range with $\mathcal{A} \sim 1$, in the weak-shear regime, as promised in § 3.2.1. To be more specific, the transition range is a poloidal-scale range $k_y^{\mathrm{o}}(\gamma_E) \lesssim k_y \lesssim k_y^{\mathrm{T}}$, wherein the fluctuations' aspect ratio increases from $\mathcal{A}(k_y^{\mathrm{o}}) \ll 1$ at the outer scale to $\mathcal{A}(k_y^{\mathrm{T}}) \sim 1$ at the end of the transition range, located at a new scale $k_y \sim k_y^{\mathrm{T}}$. Note that, by definition, free-energy injection by the linear instability is negligible at all scales below the outer scale.

First, let us show that radial wavenumbers below the outer scale cannot be determined by the tilting of the eddies by the flow shear, i.e. that k_x must be determined by nonlinear effects (with a boundary condition $k_x = k_x^{\mathrm{o}}$ at the outer scale). Consider the simpler case of $\mathcal{A}^{\mathrm{o}}(0) \ll 1$ turbulence in the presence of a flow shear of intermediate strength $\gamma_{\mathrm{c}} \ll \gamma_E \ll \gamma^{\mathrm{o}}(0)$. In this case, the radial wavenumber at the outer scale is given by (3.17):

$$k_x^{\mathrm{o}}(\gamma_E) \sim k_y^{\mathrm{o}}(0)\tau_{\mathrm{nl}}^{\mathrm{o}}(0)\gamma_E. \tag{A1}$$

Now, suppose that (A1) holds beyond the outer scale, *viz*. that

$$k_x \sim k_y \tau_{\mathrm{nl}} \gamma_E \tag{A2}$$

https://doi.org/10.1017/S0022377825000054 Published online by Cambridge University Press

for $k_y > k_y^{\mathrm{o}}$. Combining (A2) with the definition of the nonlinear time (3.1) and assuming that the free-energy flux (3.4) is constant below the outer scale, we find that, for the scales where (A2) holds,

$$\tau_{\mathrm{nl}}^{-1} \propto \gamma_E^{2/5} k_y^{4/5} \propto k_y^{4/5}. \tag{A3}$$

However, beyond the outer scale, the nonlinear mixing rate must increase faster with k_y than the injection rate $\gamma_{\boldsymbol{k}} \propto k_y$, which (A3) does not. Therefore, the assumption that (A2) holds beyond the outer scale contradicts the very definition of the outer scale that we adopted in § 3.1.

Instead, let us suppose that, due to nonlinear mixing beyond the outer scale, the radial wavenumbers corresponding to the poloidal wavenumbers in the range $k_y^{\mathrm{o}}(\gamma_E) \lesssim k_y \lesssim k_y^{\mathrm{T}}$ satisfy

$$\frac{k_x}{k_x^{\mathrm{o}}} \sim \left(\frac{k_y}{k_y^{\mathrm{o}}}\right)^{1+\lambda}. \tag{A4}$$

The parameter λ is a measure of the tendency of the nonlinear mixing to 'isotropise' (or 'anisotropise' if $\lambda < 0$) the turbulent fluctuations with increasing k_y.[13] This can also be expressed as

$$\frac{\mathcal{A}(k_y)}{\mathcal{A}^{\mathrm{o}}} \sim \left(\frac{k_y}{k_y^{\mathrm{o}}}\right)^{\lambda}. \tag{A5}$$

If $\lambda > 0$, the transition region ends at $\mathcal{A}(k_y^{\mathrm{T}}) \sim 1$, so (A5) gives us

$$k_y^{\mathrm{T}} \sim \frac{k_y^{\mathrm{o}}}{(\mathcal{A}^{\mathrm{o}})^{1/\lambda}} \gg k_y^{\mathrm{o}}. \tag{A6}$$

Inside the transition region, the expression for the nonlinear time (3.2) and the assumption of constant free-energy flux (3.4) jointly imply

$$\frac{\overline{\varphi}}{\overline{\varphi}^{\mathrm{o}}} \sim \left(\frac{k_y}{k_y^{\mathrm{o}}}\right)^{-2/3\,-\,\lambda/3}. \tag{A7}$$

Therefore, the k_y spectrum in the transition range must be steeper than the inertial-range spectrum (3.5). Using (A4), we can recast (A7) in terms of the radial wavenumbers:

$$\frac{\overline{\varphi}}{\overline{\varphi}^{\mathrm{o}}} \sim \left(\frac{k_x}{k_x^{\mathrm{o}}}\right)^{-2/3\,+\,\lambda/3(1+\lambda)}, \tag{A8}$$

which is shallower than the inertial-range spectrum (3.5).

[13] Notice that, as discussed in § 3.2.1, one possibility is that the outer-scale aspect ratio $\mathcal{A}^{\mathrm{o}}(0)$ is inherited by the inertial-range cascade in the sense that $\mathcal{A}$ in the inertial range is independent of k_y, i.e. it is scale invariant. In the analysis above, this corresponds to $\lambda = 0$. In this case, the transition range is, in fact, the entire inertial range, $\mathcal{A}$ is scale-invariant by (A5), and the spectra (A7) and (A8) agree with (3.5).

https://doi.org/10.1017/S0022377825000054 Published online by Cambridge University Press

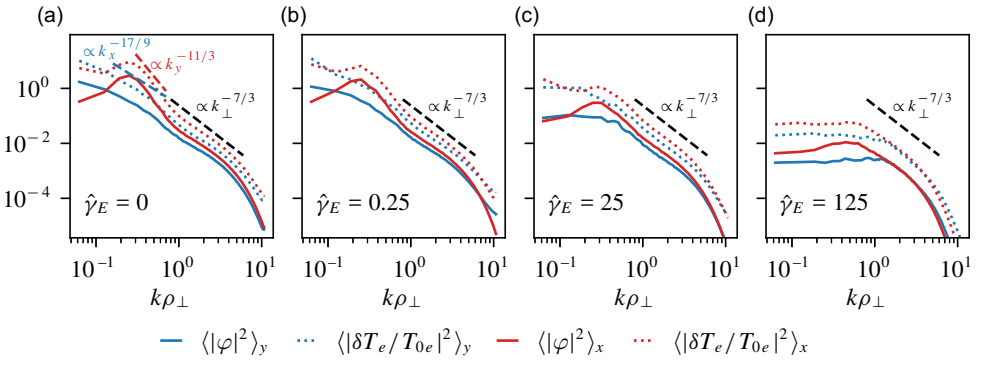


FIGURE 12. Panels (*a*)–(*d*) show the spectra (A9)–(A12), as indicated in the legend at the bottom, for the four simulations shown in figure 5. All panels show an inertial-range spectrum that agrees with the predicted $\propto k_\perp^{-7/3}$ scaling, shown as a black dashed line. In panel (*a*), where $\gamma_E = 0$ and the transition range is widest, we also show the predicted transition-range scalings in the case $\lambda = 2$ of the spectrum with k_x and k_y in blue and red dashed lines, respectively, with the exponents labelled accordingly.

We do not know how to determine λ theoretically, but we can confirm numerically that the above arguments are sound and that $\lambda > 0$. In figure 12, we show the spectra of φ and $\delta T_e/T_e$ from the ETG fluid model discussed in § 4.1 for the four Sim1 simulations with varying flow shear presented in figure 5. As a proxy for the dependence of $\overline{\varphi}$ and $\overline{\delta T_e/T_e}$ on k_x and k_y, we are using the following averages:

$$\langle|\varphi|^2\rangle_x(k_y) \equiv \sum_{k_x,k_\parallel} |\varphi_{\boldsymbol{k}}|^2, \tag{A9}$$

$$\langle|\varphi|^2\rangle_y(k_x) \equiv \sum_{k_y,k_\parallel} |\varphi_{\boldsymbol{k}}|^2, \tag{A10}$$

$$\left\langle\left|\frac{\delta T_e}{T_e}\right|^2\right\rangle_x(k_y) \equiv \sum_{k_x,k_\parallel} \left|\frac{\delta T_{e,\boldsymbol{k}}}{T_e}\right|^2, \tag{A11}$$

$$\left\langle\left|\frac{\delta T_e}{T_e}\right|^2\right\rangle_y(k_x) \equiv \sum_{k_y,k_\parallel} \left|\frac{\delta T_{e,\boldsymbol{k}}}{T_e}\right|^2. \tag{A12}$$

Note that (A9)–(A12) differ from (3.3) by a factor of k_x or k_y. Thus, the expected scalings that follow from (A7) and (A8) are

$$\langle|\varphi|^2\rangle_x \sim \left\langle\left|\frac{\delta T_e}{T_e}\right|^2\right\rangle_x \propto k_y^{-7/3\,-\,2\lambda/3}, \tag{A13}$$

$$\langle|\varphi|^2\rangle_y \sim \left\langle\left|\frac{\delta T_e}{T_e}\right|^2\right\rangle_y \propto k_x^{-7/3\,+\,2\lambda/3(1+\lambda)}. \tag{A14}$$

Figure 12(*a*) shows that the fluid-ETG spectra obtained from solving (4.1)–(4.3) with $\gamma_E = 0$ are roughly consistent with $\lambda = 2$. Increasing the value of the flow shear

https://doi.org/10.1017/S0022377825000054 Published online by Cambridge University Press

reduces the aspect ratio, as expected, and flattens the k_y spectrum to approximately match the k_x one. Unfortunately, because the aspect ratio $\mathcal{A}^o(0)$ cannot be varied in the fluid model, we are unable to vary the size of the transition range and its small span in wavenumbers limits our ability to measure λ numerically and to verify the transition-range theory laid out above with any greater accuracy. Nevertheless, our numerical results are consistent with it.

Appendix B. Numerical implementation of the fluid model

The numerical results presented in § 4.1 are obtained by solving (4.1)–(4.3) in the shearing frame

$$t' = t, \;\; x' = x, \;\; y' = y - x\gamma_E t, \;\; z' = z, \tag{B1}$$

instead of the laboratory frame (x, y, z). By using a pseudo-spectral algorithm and solving for the evolution of Fourier modes in (x', y', z'), we impose triply periodic boundary conditions in the shearing frame. The linear terms in the equations are integrated using an implicit Crank–Nicolson method, while the nonlinear ones are integrated explicitly using the Adams–Bashforth three-step method. This code is a modification of that developed and used by Ivanov *et al.* (2020); Ivanov, Schekochihin & Dorland (2022) and Adkins *et al.* (2023).

Our approach for dealing with the time-dependent radial derivatives arising from (B1) differs from the usual spectral remapping scheme that was first proposed by Hammett *et al.* (2006) for the GK code `GS2` and that forms the basis of the implementation of equilibrium flow shear in many modern gyrokinetics codes, e.g. `stella` (Barnes, Parra & Landreman 2019; St-Onge, Barnes & Parra 2022), `GKW` (Peeters *et al.* 2009) and `GENE` (Told 2012), the latter being used for the numerical simulations presented in § 4.2. While this remapping algorithm is fairly robust, the approximations that it makes can, in some cases, lead to unphysical results (McMillan, Ball & Brunner 2019). Even though steps can be taken to improve the algorithm (McMillan *et al.* 2019; Christen, Barnes & Parra 2021), the simplicity of (4.1)–(4.3) allows us to take a different, both simpler and more robust, approach. We consider a fixed (k'_x, k'_y) grid of shearing-frame wavenumbers, which corresponds to continuously drifting laboratory-frame radial wavenumbers $k_x = k'_x - \gamma_E k'_y t$ that are periodic (in time) on the interval $-K_x \leqslant k_x \leqslant K_x$, where $K_x \equiv \pi N_x/L_x$, L_x is the radial box size and N_x is the 'padded' number of radial wavenumbers. By ensuring that $N_x \geqslant \lfloor 3n_x/2 \rfloor$, where n_x is the number of resolved radial wavenumbers, we eliminate aliasing issues in the pseudo-spectral method by zeroing out all modes with $|k_x| > k_{x,\max} \equiv \pi n_x/L_x$ – this is the standard '2/3 rule' (Orszag 1971). For example, the simulations in the Sim2 set (see table 1) have $n_x = 683$ and $N_x = 1024$.

This scheme leads to a minor complication that is not encountered if one uses the remapping algorithm instead. To understand this, consider that, even in the presence of flow shear, the fluctuation amplitudes peak near $k_x = 0$ and are suppressed at large $|k_x|$ because the dissipation terms (whether physical or numerical) are determined by the laboratory-frame wavenumber k_x, not by the shearing-frame one k'_x. Thus, the appropriate choice for a Galerkin truncation, required by any pseudo-spectral algorithm, should be based on the laboratory-frame wavenumbers. This laboratory-frame truncation, along with the necessary zero padding for dealiasing, is illustrated in figure 13(*a*) in the case of zero flow shear. However, for $\gamma_E \neq 0$, we wish to solve the equations in terms of k'_x rather than k_x. To do this, we assign a

https://doi.org/10.1017/S0022377825000054 Published online by Cambridge University Press

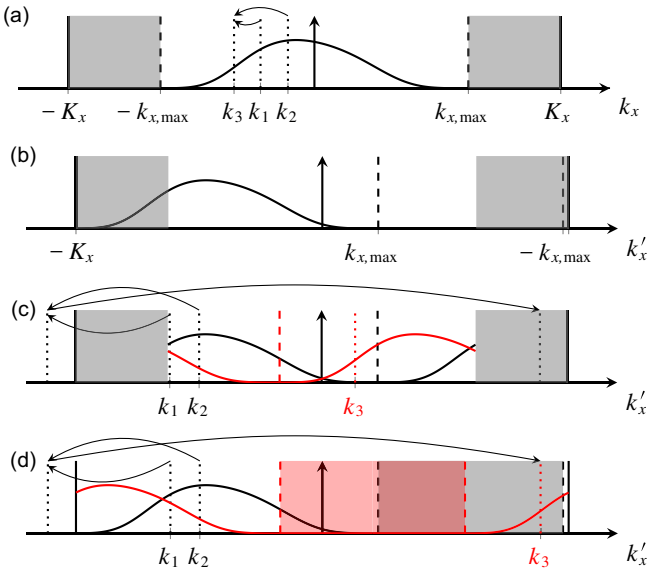


FIGURE 13. (*a*) Typical fluctuation amplitudes of sheared turbulence with $k_y = q$ for some fixed q (note that the spectrum does not peak at $k_x = 0$ if $\gamma_E \neq 0$) as a function of the laboratory-frame radial wavenumber k_x. The shaded regions indicate the zero padding needed for dealiasing. The vertical solid and vertical dashed lines denote $\pm K_x$ and $\pm k_{x,\max}$, respectively. Two radial wavenumbers, k_1 and k_2, are shown, together with $k_3 = k_1 + k_2$ into which they couple nonlinearly. (*b*) The same fluctuation amplitudes as in panel (*a*), but now transformed to the shearing frame using (B2), while keeping the padded region fixed to the outer 1/3 of the wavenumbers in the shearing frame. (*c*) Same as in panel (*b*) but with k_x made periodic on $[-k_{x,\max}, k_{x,\max}]$ and computed via (B3) instead. The fluctuation amplitudes with $k_y = 2q$ are shown in red. Here, k_1 and k_2 are the same two modes as in panel (*a*) that couple nonlinearly into k_3 (shown in red as the corresponding poloidal wavenumber is $k_y = 2q$). However, in this version of dealiasing, their sum falls into the dealiased region. (*d*) The correct way to represent the fluctuations in the shearing frame using (B2) and zeroing out modes with $|k_x| > k_{x,\max}$. We are showing the same two wavenumbers k_1 and k_2 as before. They couple nonlinearly to modes with $(k_x, k_y) = (k_3, 2q)$, whose fluctuation amplitudes and dealiased regions are shown in red. In panels (*c*) and (*d*), to illustrate the correspondence between modes with $k_y = q$ and $k_y = 2q$, we have used the exact same function of k_x to represent fluctuation amplitudes at both poloidal wavenumbers.

laboratory-frame k_x to each k_x' using

$$k_x = k_x' - \gamma_E k_y' t + \frac{2\pi N_x m}{L_x}, \tag{B2}$$

where m is an integer chosen so that $-K_x \leqslant k_x \leqslant K_x$. Figure 13(*b*) shows that using (B2) naïvely can (depending on how much k_x has drifted) bring physically meaningful small-$|k_x|$ modes into the region where the amplitudes are zeroed out to avoid aliasing. Effectively, this naïve method offsets the interval of resolved laboratory-frame modes so that, for any given $k_y \neq 0$, it is no longer centred around $k_x = 0$. Therefore, this approach does not work. One alternative is to consider instead k_x that drifts periodically as

$$k_x = k_x' - \gamma_E k_y' t + \frac{2\pi n_x m}{L_x}, \tag{B3}$$

https://doi.org/10.1017/S0022377825000054 Published online by Cambridge University Press

where now m is chosen so that $-k_{x,\max} \leqslant k_x \leqslant k_{x,\max}$, i.e. the radial wavenumbers drift periodically only within the physically resolved interval $[-k_{x,\max}, k_{x,\max}]$, instead of the larger 'padded' interval $[-K_x, K_x]$. However, this method is not suitable for calculating the nonlinear terms: as figure 13(*c*) shows, it removes physically meaningful nonlinear couplings. Similarly, one can also show that it also introduces aliasing-like couplings between physically unrelated modes (e.g. one can choose modes with $k_1,\ k_2 > 0$ that are nonlinearly coupled to $k_1 + k_2 - 2\pi n_x/L_x < 0$). The correct approach, which employs (B2) and dealiasing based on $|k_x|$, is demonstrated in figure 13(*d*). This requires keeping track of the laboratory-frame k_x and zeroing out modes based on it. Fortunately, this is straightforward to do and the additional overhead of having to compute the inverse of the linear response, required for the implicit Crank–Nicolson method, is negligible for the simple fluid model.

Note that continuously drifting wavenumbers have one extra advantage over the remapping algorithm. A mode that has been sheared so much that it re-emerges at the other side of the resolved wavenumber interval has necessarily passed through the dealiased region. Thus, its amplitude is zero and so cannot introduce any spurious fluctuations.

This algorithm is effectively the same as that used by Lithwick (2007) (and attributed by him to Gordon Ogilvie) for simulations of hydrodynamic sheared flows.

Appendix C. Momentum flux in the fluid ETG model

We want to compute the radial flux of poloidal momentum,

$$\Pi \equiv \sum_s m_s \int \frac{\mathrm{d}^3\boldsymbol{r}}{V} \int \mathrm{d}^3\boldsymbol{w}\ (\boldsymbol{v}_E \cdot \nabla x)(\boldsymbol{w} \cdot \nabla y)\delta f_s, \tag{C1}$$

in the fluid ETG model used in § 4.1 and § 5. The details of the derivation of the model can be found in Appendix B of Adkins *et al.* (2023). Here, we require only a few facts about the limit in which this derivation was carried out.

First, the ion gyroradius is large, *viz.* $k_\perp \rho_i \gg 1$, which allows us to neglect h_i in the ion distribution function δf_i given by (2.2), so

$$\delta f_i \approx -\frac{Ze\phi}{T_i} F_i. \tag{C2}$$

This implies that the ion contribution to (C1) vanishes:

$$\int \frac{\mathrm{d}^3\boldsymbol{r}}{V} \int \mathrm{d}^3\boldsymbol{w}\ (\boldsymbol{v}_E \cdot \nabla x)(\boldsymbol{w} \cdot \nabla y)\delta f_i \propto \int \frac{\mathrm{d}^3\boldsymbol{r}}{V} \frac{\partial \phi}{\partial y}\phi = 0. \tag{C3}$$

Second, the electron distribution function is expressed as

$$\delta f_e = \varphi F_e + h_e, \tag{C4}$$

where $\varphi = e\phi/T_e$ and h_e is gyroangle independent at fixed $\boldsymbol{R}_e = \boldsymbol{r} - \hat{\boldsymbol{z}} \times \boldsymbol{w}/\Omega_e$. Since the radial $\boldsymbol{E} \times \boldsymbol{B}$ velocity is

$$\boldsymbol{v}_E \cdot \nabla x = -\frac{1}{2}\rho_e v_{\mathrm{the}} \frac{\partial \varphi}{\partial y}, \tag{C5}$$

https://doi.org/10.1017/S0022377825000054 Published online by Cambridge University Press

(C1) becomes

$$\Pi = -\frac{1}{2}\rho_e m_e v_{\mathrm{the}} \int \frac{\mathrm{d}^3\boldsymbol{r}}{V} \int \mathrm{d}^3\boldsymbol{w}\, \frac{\partial \varphi}{\partial y}(\boldsymbol{w}\cdot\nabla y) h_e, \tag{C6}$$

where the contribution from the φF_e part of (C4) has vanished. Evaluating (C6) is a standard GK calculation, which we outline now.

Noting that the perpendicular part of $\boldsymbol{w}$ is

$$\boldsymbol{w}_\perp = w_\perp(\cos\theta\hat{\boldsymbol{x}} - \sin\theta\hat{\boldsymbol{y}}), \tag{C7}$$

where θ is the gyroangle, and that

$$\hat{\boldsymbol{z}} \times \boldsymbol{w}_\perp = -\frac{\partial \boldsymbol{w}_\perp}{\partial\theta}, \tag{C8}$$

we find

$$\int \mathrm{d}^3\boldsymbol{w}\, \boldsymbol{w}_\perp h_e = \int \mathrm{d}^3\boldsymbol{w}\, \hat{\boldsymbol{z}} \times \frac{\partial \boldsymbol{w}_\perp}{\partial\theta} h_e = -\int \mathrm{d}^3\boldsymbol{w}\, \hat{\boldsymbol{z}} \times \boldsymbol{w}_\perp \frac{\partial h_e}{\partial\theta}. \tag{C9}$$

As h_e is independent of θ at fixed $\boldsymbol{R}_e$, the last partial derivative in (C9) (which is evaluated at fixed $\boldsymbol{r}$) becomes

$$\frac{\partial h_e}{\partial\theta} = \frac{\partial}{\partial\theta}\left(-\frac{\hat{\boldsymbol{z}}\times\boldsymbol{w}}{\Omega_e}\right)\cdot\frac{\partial h_e}{\partial \boldsymbol{R}_e} = -\frac{\boldsymbol{w}_\perp}{\Omega_e}\cdot\frac{\partial h_e}{\partial \boldsymbol{R}_e}. \tag{C10}$$

Substituting (C10) into (C9), dotting by ∇y, and making use of

$$\frac{1}{2\pi}\int_0^{2\pi} \mathrm{d}\theta\, w_i w_j = \frac{w_\perp^2}{2}(\delta_{ij} - \hat{z}_i\hat{z}_j) + w_\parallel^2 \hat{z}_i\hat{z}_j, \tag{C11}$$

we find

$$\int \mathrm{d}^3\boldsymbol{w}\, (\boldsymbol{w}\cdot\nabla y) h_e = \int \mathrm{d}^3\boldsymbol{w}\, \frac{w_\perp^2}{2\Omega_e}\frac{\partial h_e}{\partial x}. \tag{C12}$$

Then, using $v_{\mathrm{the}}/\Omega_e = -\rho_e$ and (C12), (C6) reduces to

$$\Pi = \frac{\rho_e^2 m_e}{4}\int \frac{\mathrm{d}^3\boldsymbol{r}}{V}\int \mathrm{d}^3\boldsymbol{w}\, \frac{\partial\varphi}{\partial y} w_\perp^2 \frac{\partial h_e}{\partial x}. \tag{C13}$$

Finally, to lowest order in $k_\perp\rho_e \ll 1$, h_e is given by (Adkins *et al.* 2023)

$$h_e = \left[\frac{\delta n_e}{n_e} - \varphi + \frac{\delta T_e}{T_e}\left(\frac{w^2}{v_{\mathrm{the}}^2} - \frac{3}{2}\right)\right] F_e, \tag{C14}$$

where the density perturbation is given by (4.5). Therefore, (C13) becomes

$$\Pi = -\frac{n_e T_e \rho_e^2}{2}\int \frac{\mathrm{d}^3\boldsymbol{r}}{V}\frac{\partial\varphi}{\partial y}\frac{\partial}{\partial x}\left[\left(1 + \frac{ZT_e}{T_i}\right)\varphi - \frac{\delta T_e}{T_e}\right] \tag{C15}$$

to lowest order in $k_\perp\rho_e \ll 1$, which is exactly (5.2).

https://doi.org/10.1017/S0022377825000054 Published online by Cambridge University Press

REFERENCES

ABEL, I.G., PLUNK, G.G., WANG, E., BARNES, M., COWLEY, S.C., DORLAND, W. & SCHEKOCHIHIN, A.A. 2013 Multiscale gyrokinetics for rotating tokamak plasmas: fluctuations, transport and energy flows. *Rep. Prog. Phys.* **76** (11), 116201.

ADKINS, T., IVANOV, P.G. & SCHEKOCHIHIN, A.A. 2023 Scale invariance and critical balance in electrostatic drift-kinetic turbulence. *J. Plasma Phys.* **89** (4), 905890406.

ADKINS, T., SCHEKOCHIHIN, A.A., IVANOV, P.G. & ROACH, C.M. 2022 Electromagnetic instabilities and plasma turbulence driven by electron-temperature gradient. *J. Plasma Phys.* **88** (4), 905880410.

AJAY, C.J., BRUNNER, S., & BALL, J. 2021 Effect of collisions on non-adiabatic electron dynamics in ITG-driven microturbulence. *Phys. Plasmas* **28** (9), 092303.

ARTUN, M. & TANG, W.M. 1992 Gyrokinetic analysis of ion temperature gradient modes in the presence of sheared flows. *Phys. Fluids B* **4** (5), 1102–1114.

BARNES, M., ABEL, I.G., DORLAND, W., ERNST, D.R., HAMMETT, G.W., RICCI, P., ROGERS, B.N., SCHEKOCHIHIN, A.A. & TATSUNO, T. 2009 Linearized model fokker-planck collision operators for gyrokinetic simulations II. Numerical Implementation and Tests. *Phys. Plasmas* **16**, 072107.

BARNES, M., PARRA, F.I. & LANDREMAN, M. 2019 `stella`: an operator-split, implicit–explicit δf-gyrokinetic code for general magnetic field configurations. *J. Comput. Phys.* **391**, 365.

BARNES, M., PARRA, F.I., HIGHCOCK, E.G., SCHEKOCHIHIN, A.A., COWLEY, S.C. & ROACH, C.M. 2011 Turbulent transport in tokamak plasmas with rotational shear. *Phys. Rev. Lett.* **106** (17), 175004.

BARNES, M., PARRA, F.I. & SCHEKOCHIHIN, A.A. 2011 Critically balanced ion temperature gradient turbulence in fusion plasmas. *Phys. Rev. Lett.* **107** (11), 115003.

BIGLARI, H., DIAMOND, P.H. & TERRY, P.W. 1990 Influence of sheared poloidal rotation on edge turbulence. *Phys. Fluids B* **2** (1), 1–4.

BOLDYREV, S. 2006 Spectrum of magnetohydrodynamic turbulence. *Phys. Rev. Lett.* **96** (11), 115002.

BOLDYREV, S., MASON, J. & CATTANEO, F. 2009 Dynamic alignment and exact scaling laws in magnetohydrodynamic turbulence. *Astrophys. J.* **699** (1), L39–L42.

BRAGINSKII, S.I. 1965 Transport processes in a plasma. *Rev. Plasma Phys.* **1**, 205.

CANDY, J., WALTZ, R.E., FAHEY, M.R. & HOLLAND, C. 2007 The effect of ion-scale dynamics on electron-temperature-gradient turbulence. *Plasma Phys. Control. Fusion* **49** (8), 1209–1220.

CASSON, F.J., PEETERS, A.G., CAMENEN, Y., HORNSBY, W.A., SNODIN, A.P., STRINTZI, D. & SZEPESI, G. 2009 Anomalous parallel momentum transport due to E×B flow shear in a tokamak plasma. *Phys. Plasmas* **16**, 092303.

CATTO, P.J. 2019 Practical gyrokinetics. *J. Plasma Phys.* **85** (03), 925850301.

CATTO, P.J., ROSENBLUTH, M.N. & LIU, C.S. 1973 Parallel velocity shear instabilities in an inhomogeneous plasma with a sheared magnetic field. *Phys. Fluids* **16** (10), 1719–1729.

CHRISTEN, N., BARNES, M., HARDMAN, M.R. & SCHEKOCHIHIN, A.A. 2022 Bistable turbulence in strongly magnetised plasmas with a sheared mean flow. *J. Plasma Phys.* **88** (5), 905880504.

CHRISTEN, N., BARNES, M. & PARRA, F.I. 2021 Continuous-in-time approach to flow shear in a linearly implicit local δf gyrokinetic code. *J. Plasma Phys.* **87**, 905870230.

COLYER, G.J., SCHEKOCHIHIN, A.A., PARRA, F.I., ROACH, C.M., BARNES, M.A., GHIM, Y.-C. & DORLAND, W. 2017 Collisionality scaling of the electron heat flux in ETG turbulence. *Plasma Phys. Control. Fusion* **59** (5), 055002.

COOPER, W.A. 1988 Ballooning instabilities in tokamaks with sheared toroidal flows. *Plasma Phys. Control. Fusion* **30** (13), 1805–1812.

DIAMOND, P.H., ITOH, S.-I., ITOH, K. & HAHM, T.S. 2005 Zonal flows in plasma—a review. *Plasma Phys. Control. Fusion* **47** (5), 35–R161.

DIF-PRADALIER, G., DIAMOND, P.H., GRANDGIRARD, V., SARAZIN, Y., ABITEBOUL, J., GARBET, X., GHENDRIH, P., STRUGAREK, A., KU, S. & CHANG, C.S. 2010 On the validity of the local diffusive paradigm in turbulent plasma transport. *Phys. Rev. E* **82** (2), 025401.

DIF-PRADALIER, G. *et al.* 2015 Finding the elusive E × B staircase in magnetized plasmas. *Phys. Rev. Lett.* **114**, 085004.

DIMITS, A.M. *et al.* 2000 Comparisons and physics basis of tokamak transport models and turbulence simulations. *Phys. Plasmas* **7** (3), 969–983.

https://doi.org/10.1017/S0022377825000054 Published online by Cambridge University Press

DORLAND, W., JENKO, F., KOTSCHENREUTHER, M. & ROGERS, B.N. 2000 Electron temperature gradient turbulence. *Phys. Rev. Lett.* **85** (26), 5579–5582.

DRAKE, J.F., GUZDAR, P.N. & HASSAM, A.B. 1988 Streamer formation in plasma with a temperature gradient. *Phys. Rev. Lett.* **61** (19), 2205–2208.

DUPREE, T.H. 1972 Theory of phase space density granulation in plasma. *Phys. Fluids* **15** (2), 334–344.

FEDORCZAK, N., GHENDRIH, P., HENNEQUIN, P., TYNAN, G.R., DIAMOND, P.H. & MANZ, P. 2013 Dynamics of tilted eddies in a transversal flow at the edge of tokamak plasmas and the consequences for L–H transition. *Plasma Phys. Control. Fusion* **55** (12), 124024.

FIELD, A.R., MICHAEL, C., AKERS, R.J., CANDY, J., COLYER, G., GUTTENFELDER, W., GHIM, Y.-C, ROACH, C.M., SAARELMA, S., & The MAST Team 2011 Plasma rotation and transport in MAST spherical tokamak. *Nucl. Fusion* **51** (6), 063006.

FOX, M.F.J., VAN WYK, F, FIELD, A.R., GHIM, Y-C, PARRA, F.I., SCHEKOCHIHIN, A.A., & The MAST team 2017 Symmetry breaking in MAST plasma turbulence due to toroidal flow shear. *Plasma Phys. Control. Fusion* **59** (3), 034002.

GHIM, Y.-C, FIELD, A.R., SCHEKOCHIHIN, A.A., HIGHCOCK, E.G., MICHAEL, C., & The MAST team 2014 Local dependence of ion temperature gradient on magnetic configuration, rotational shear and turbulent heat flux in MAST. *Nucl. Fusion* **54** (4), 042003.

GHIM, Y.-C., SCHEKOCHIHIN, A.A., FIELD, A.R., ABEL, I.G., BARNES, M., COLYER, G., COWLEY, S.C., PARRA, F.I., DUNAI, D. & ZOLETNIK, S. 2013 Experimental signatures of critically balanced turbulence in MAST. *Phys. Rev. Lett.* **110** (14), 145002.

GOLDREICH, P. & SRIDHAR, S. 1995 Toward a theory of interstellar turbulence. 2: strong Alfvénic turbulence. *Astrophys. J.* **438**, 763.

HAMMETT, G.W., BEER, M.A., DORLAND, W., COWLEY, S.C. & SMITH, S.A. 1993 Developments in the gyrofluid approach to tokamak turbulence simulations. *Plasma Phys. Control. Fusion* **35** (8), 973–985.

HAMMETT, G.W., DORLAND, W., LOUREIRO, N.F. & TATSUNO, T. 2006 Implementation of large scale ExB shear flow in the GS2 gyrokinetic turbulence code.**48**, VP1.136.

HARDMAN, M.R., BARNES, M. & ROACH, C.M. 2020 Stabilisation of short-wavelength instabilities by parallel-to-the-field shear in long-wavelength $E \times B$ flows. *J. Plasma Phys.* **86**, 905860601.

HARDMAN, M.R., BARNES, M., ROACH, C.M. & PARRA, F.I. 2019 A scale-separated approach for studying coupled ion and electron scale turbulence. *Plasma Phys. Control. Fusion* **61** (6), 065025.

HATCH, D.R., HAZELTINE, R.D., KOTSCHENREUTHER, M.K. & MAHAJAN, S.M. 2018 Flow shear suppression of pedestal ion temperature gradient turbulence-a first principles theoretical framework. *Plasma Phys. Control. Fusion* **60** (8), 084003.

HELANDER, P. & PLUNK, G.G. 2022 Energetic bounds on gyrokinetic instabilities. Part 1 Fundamentals. *J. Plasma Phys.* **88** (2), 905880207.

HIGHCOCK, E.G., BARNES, M., PARRA, F.I., SCHEKOCHIHIN, A.A., ROACH, C.M. & COWLEY, S.C. 2011 Transport bifurcation induced by sheared toroidal flow in tokamak plasma. *Phys. Plasmas* **18** (10), 102304.

HIGHCOCK, E.G., BARNES, M., SCHEKOCHIHIN, A.A., PARRA, F.I., ROACH, C.M. & COWLEY, S.C. 2010 Transport bifurcation in a rotating tokamak plasma. *Phys. Rev. Lett.* **105** (21), 215003.

HIGHCOCK, E.G., SCHEKOCHIHIN, A.A., COWLEY, S.C., BARNES, M., PARRA, F.I., ROACH, C.M. & DORLAND, W. 2012 Zero-turbulence manifold in a toroidal plasma. *Phys. Rev. Lett.* **109** (26), 265001.

HOBBS, C.G., HOUSE, M.G., LEBOEUF, J.N., DAWSON, J.M., DECYK, V.K., KISSICK, M.W. & SYDORA, R.D. 2001 Effect of sheared toroidal rotation on ion temperature gradient turbulence and resistive kink stability in a large aspect ratio tokamak. *Phys. Plasmas* **8** (11), 4849–4855.

HOFFMANN, A.C.D., FREI, B.J. & RICCI, P. 2023 Gyrokinetic moment-based simulations of the dimits shift. *J. Plasma Phys.* **89** (6), 905890611.

HOLLAND, C. & DIAMOND, P.H. 2004 A simple model of interactions between electron temperature gradient and drift-wave turbulence. *Phys. Plasmas* **11** (3), 1043–1051.

HOWARD, N.T., HOLLAND, C., WHITE, A.E., GREENWALD, M. & CANDY, J. 2016*a* Multi-scale gyrokinetic simulation of tokamak plasmas: enhanced heat loss due to cross-scale coupling of plasma turbulence. *Nucl. Fusion* **56** (1), 014004.

https://doi.org/10.1017/S0022377825000054 Published online by Cambridge University Press

HOWARD, N.T., HOLLAND, C., WHITE, A.E., GREENWALD, M., CANDY, J. & CREELY, A.J. 2016b Multi-scale gyrokinetic simulations: comparison with experiment and implications for predicting turbulence and transport. *Phys. Plasmas* **23** (5), 056109.

IVANOV, P.G., SCHEKOCHIHIN, A.A. & DORLAND, W. 2022 Dimits transition in three-dimensional ion-temperature-gradient turbulence. *J. Plasma Phys.* **88** (5), 905880506.

IVANOV, P.G., SCHEKOCHIHIN, A.A., DORLAND, W., FIELD, A.R. & PARRA, F.I. 2020 Zonally dominated dynamics and Dimits threshold in curvature-driven ITG turbulence. *J. Plasma Phys.* **86** (5), 855860502.

JENKO, F. 2000 Massively parallel Vlasov simulation of electromagnetic drift-wave turbulence. *Comput. Phys. Commun.* **125** (1-3), 196–209.

JENKO, F. 2006 Streamer saturation: a dynamical systems approach. *Phys. Lett. A* **351** (6), 417–423.

JENKO, F., DORLAND, W., KOTSCHENREUTHER, M. & ROGERS, B.N. 2000 Electron temperature gradient driven turbulence. *Phys. Plasmas* **7** (5), 1904–1910.

KOBAYASHI, S. & ROGERS, B.N. 2012 The quench rule, Dimits shift, and eigenmode localization by small-scale zonal flows. *Phys. Plasmas* **19** (1), 012315.

KOLMOGOROV, A.N. 1941 Local structure of turbulence in incompressible viscous fluid at very large Reynolds numbers. *Dokl. Akad. Nauk SSSR* **30**, 299.

LI, P.-Y., TERRY, P.W., WHELAN, G.G. & PUESCHEL, M.J. 2021 Saturation physics of threshold heat-flux reduction. *Phys. Plasmas* **28** (10), 102507.

LIN, Z., HAHM, T.S., LEE, W.W., TANG, W.M. & DIAMOND, P.H. 1999 Effects of collisional zonal flow damping on turbulent transport. *Phys. Rev. Lett.* **83** (18), 3645–3648.

LIPPERT, M., RATH, F. & PEETERS, A.G. 2023 Size convergence of the E × B staircase pattern in flux tube simulations of ion temperature gradient-driven turbulence. *Phys. Plasmas* **30**, 074501.

LITHWICK, Y. 2007 Nonlinear evolution of hydrodynamical shear flows in two dimensions. *Astrophys. J.* **670** (1), 789–804.

MAEYAMA, S., IDOMURA, Y., WATANABE, T.H., NAKATA, M., YAGI, M., MIYATO, N., ISHIZAWA, A. & NUNAMI, M. 2015 Cross-scale interactions between electron and ion scale turbulence in a tokamak plasma. *Phys. Rev. Lett.* **114** (25), 255002.

MALLET, A. & SCHEKOCHIHIN, A.A. 2017 A statistical model of three-dimensional anisotropy and intermittency in strong Alfvénic turbulence. *Mon. Not. R. Astron. Soc.* **466** (4), 3918–3927.

MALLET, A., SCHEKOCHIHIN, A.A., CHANDRAN, B.D.G., CHEN, C.H.K., HORBURY, T.S., WICKS, R.T. & GREENAN, C.C. 2016 Measures of three-dimensional anisotropy and intermittency in strong Alfvénic turbulence. *Mon. Not. R. Astron. Soc.* **459** (2), 2130–2139.

MANTICA, P. *et al.* 2009 Experimental study of the ion critical-gradient length and stiffness level and the impact of rotation in the jet tokamak. *Phys. Rev. Lett.* **102** (17), 175002.

MCKEE, G.R. *et al.* 2009 Dependence of the L- to H-mode power threshold on toroidal rotation and the link to edge turbulence dynamics. *Nucl. Fusion* **49** (11), 115016.

MCMILLAN, B.F., BALL, J. & BRUNNER, S. 2019 Simulating background shear flow in local gyrokinetic simulations. *Plasma Phys. Control. Fusion* **61** (5), 055006.

MCMILLAN, B.F., JOLLIET, S., TRAN, T.M., VILLARD, L., BOTTINO, A. & ANGELINO, P. 2009 Avalanchelike bursts in global gyrokinetic simulations. *Phys. Plasmas* **16** (2), 022310.

MCMILLAN, B.F., PRINGLE, C.C.T., & TEACA, B. 2018 Simple advecting structures and the edge of chaos in subcritical tokamak plasmas. *J. Plasma Phys.* **84** (6).

NAZARENKO, S.V. & SCHEKOCHIHIN, A.A. 2011 Critical balance in magnetohydrodynamic, rotating and stratified turbulence: towards a universal scaling conjecture. *J. Fluid Mech.* **677**, 134–153.

NEWTON, S.L., COWLEY, S.C. & LOUREIRO, N.F. 2010 Understanding the effect of sheared flow on microinstabilities. *Plasma Phys. Control. Fusion* **52** (12), 125001.

NIES, R., PARRA, F.I., BARNES, M., MANDELL, N. & DORLAND, W. 2024 Saturation of magnetised plasma turbulence by propagating zonal flows, arXiv: 2409.02283.

ORSZAG, S.A. 1971 On the elimination of aliasing in finite-difference schemes by filtering high-wavenumber components. *J. Atmos. Sci.* **28** (6), 1074–1074.

PARISI, J.F. *et al.* 2020 Toroidal and slab ETG instability dominance in the linear spectrum of JET-ILW pedestals. *Nucl. Fusion* **60** (12), 126045.

https://doi.org/10.1017/S0022377825000054 Published online by Cambridge University Press

PARISI, J.F. *et al.* 2022 Three-dimensional inhomogeneity of electron-temperature-gradient turbulence in the edge of tokamak plasmas. *Nucl. Fusion* **62** (8), 086045.

PARRA, F.I., BARNES, M., HIGHCOCK, E.G., SCHEKOCHIHIN, A.A. & COWLEY, S.C. 2011a Momentum injection in tokamak plasmas and transitions to reduced transport. *Phys. Rev. Lett.* **106** (11), 115004.

PARRA, F.I., BARNES, M. & PEETERS, A.G. 2011b Up-down symmetry of the turbulent transport of toroidal angular momentum in tokamaks. *Phys. Plasmas* **18** (6), 062501.

PEETERS, A.G., CAMENEN, Y., CASSON, F.J., HORNSBY, W.A., SNODIN, A.P., STRINTZI, D. & SZEPESI, G. 2009 The nonlinear gyro-kinetic flux tube code GKW. *Comput. Phys. Commun.* **180** (12), 2650–2672.

PEETERS, A.G., RATH, F., BUCHHOLZ, R., CAMENEN, Y., CANDY, J., CASSON, F.J., GROSSHAUSER, S.R., HORNSBY, W.A., STRINTZI, D. & WEIKL, A. 2016 Gradient-driven flux-tube simulations of ion temperature gradient turbulence close to the non-linear threshold. *Phys. Plasmas* **23** (8), 082517.

PRINGLE, C.C.T., MCMILLAN, B.F. & TEACA, B. 2017 A nonlinear approach to transition in subcritical plasmas with sheared flow. *Phys. Plasmas* **24** (12), 122307.

ROACH, C.M. *et al.* 2009 Gyrokinetic simulations of spherical tokamaks. *Plasma Phys. Control. Fusion* **51** (12), 124020.

ROGERS, B.N., DORLAND, W. & KOTSCHENREUTHER, M. 2000 Generation and stability of zonal flows in ion-temperature-gradient mode turbulence. *Phys. Rev. Lett.* **85** (25), 5336–5339.

SARAZIN, Y. *et al.* 2021 Key impact of phase dynamics and diamagnetic drive on reynolds stress in magnetic fusion plasmas. *Plasma Phys. Control. Fusion* **63** (6), 064007.

SCHEKOCHIHIN, A.A. 2022 MHD turbulence: a biased review. *J. Plasma Phys.* **88** (5), 155880501.

SCHEKOCHIHIN, A.A., COWLEY, S.C., DORLAND, W., HAMMETT, G.W., HOWES, G.G., QUATAERT, E. & TATSUNO, T. 2009 Astrophysical gyrokinetics: kinetic and fluid turbulent cascades in magnetized weakly collisional plasmas. *Astrophys. J.* **182**, 310.

SCHEKOCHIHIN, A.A., HIGHCOCK, E.G. & COWLEY, S.C. 2012 Subcritical fluctuations and suppression of turbulence in differentially rotating gyrokinetic plasmas. *Plasma Phys. Control. Fusion* **54** (5), 055011.

SEIFERLING, F., PEETERS, A.G., GROSSHAUSER, S.R., RATH, F. & WEIKL, A. 2019 The interplay of an external torque and E×B structure formation in tokamak plasmas. *Phys. Plasmas* **26**, 102306.

SHAING, K.C., CRUME, E.C., Jr. & HOULBERG, W.A. 1990 Bifurcation of poloidal rotation and suppression of turbulent fluctuations: a model for the L–H transition in tokamaks. *Phys. Fluids B* **2** (6), 1492–1498.

SMOLYAKOV, A.I., DIAMOND, P.H. & MEDVEDEV, M.V. 2000 Role of ion diamagnetic effects in the generation of large scale flows in toroidal ion temperature gradient mode turbulence. *Phys. Plasmas* **7** (10), 3987–3992.

ST-ONGE, D.A., BARNES, M. & PARRA, F.I. 2022 A novel approach to radially global gyrokinetic simulation using the flux-tube code `stella`. *J. Comput. Phys* **468**, 111498.

SUGAMA, H., WATANABE, T.H., NUNAMI, M. & NISHIMURA, S. 2011 Momentum balance and radial electric fields in axisymmetric and nonaxisymmetric toroidal plasmas. *Plasma Phys. Control. Fusion* **53** (2), 024004.

SYNAKOWSKI, E.J. *et al.* 1997 Roles of electric field shear and Shafranov shift in sustaining high confinement in enhanced reversed shear plasmas on the TFTR tokamak. *Phys. Rev. Lett.* **78** (15), 2972–2975.

TIRKAS, S., CHEN, H., MERLO, G., JENKO, F. & PARKER, S. 2023 Zonal flow excitation in electron-scale tokamak turbulence. *Nucl. Fusion* **63** (2), 026015.

TOLD, D. 2012 Gyrokinetic microturbulence in transport barriers. *PhD thesis*. Universität Ulm. Germany.

VOLČOKAS, A., BALL, J. & BRUNNER, S. 2022 Ultra long turbulent eddies, magnetic topology, and the triggering of internal transport barriers in tokamaks. *Nucl. Fusion* **63** (1), 014003.

WAELBROECK, F.L. & CHEN, L. 1991 Ballooning instabilities in tokamaks with sheared toroidal flows. *Phys. Fluids B* **3** (3), 601–610.

WALTZ, R.E., CANDY, J. & FAHEY, M. 2007 Coupled ion temperature gradient and trapped electron mode to electron temperature gradient mode gyrokinetic simulations. *Phys. Plasmas* **14** (5), 056116.

https://doi.org/10.1017/S0022377825000054 Published online by Cambridge University Press

WALTZ, R.E., DEWAR, R.L. & GARBET, X. 1998 Theory and simulation of rotational shear stabilization of turbulence. *Phys. Plasmas* **5** (5), 1784–1792.

WALTZ, R.E., KERBEL, G.D. & MILOVICH, J. 1994 Toroidal gyro-Landau fluid model turbulence simulations in a nonlinear ballooning mode representation with radial modes. *Phys. Plasmas* **1** (7), 2229–2244.

VAN WYK, F., HIGHCOCK, E.G., FIELD, A.R., ROACH, C.M., SCHEKOCHIHIN, A.A., PARRA, F.I. & DORLAND, W. 2017 Ion-scale turbulence in MAST: anomalous transport, subcritical transitions, and comparison to BES measurements. *Plasma Phys. Control. Fusion* **59** (11), 114003.

VAN WYK, F., HIGHCOCK, E.G., SCHEKOCHIHIN, A.A., ROACH, C.M., FIELD, A.R. & DORLAND, W. 2016 Transition to subcritical turbulence in a tokamak plasma. *J. Plasma Phys.* **82** (6), 905820609.

ZHANG, Y.Z. & MAHAJAN, S.M. 1992 Edge turbulence scaling with shear flow. *Phys. Fluids B* **4** (6), 1385–1387.

ZHANG, Y.Z. & MAHAJAN, S.M. 1993 Correlation theory of a two-dimensional plasma turbulence with shear flow. *Phys. Fluids B* **5** (7), 2000–2020.

ZHOU, M., LOUREIRO, N.F. & UZDENSKY, D.A. 2020 Multi-scale dynamics of magnetic flux tubes and inverse magnetic energy transfer. *J. Plasma Phys.* **86** (4), 535860401.

ZHOU, Y., ZHU, H. & DODIN, I.Y. 2019 Formation of solitary zonal structures via the modulational instability of drift waves. *Plasma Phys. Control. Fusion* **61** (7), 075003.

ZHU, H., ZHOU, Y. & DODIN, I.Y. 2020*a* Theory of the tertiary instability and the Dimits shift from reduced drift-wave models. *Phys. Rev. Lett.* **124** (5), 055002.

ZHU, H., ZHOU, Y. & DODIN, I.Y. 2020*b* Theory of the tertiary instability and the Dimits shift within a scalar model. *J. Plasma Phys.* **86** (4), 905860405.

https://doi.org/10.1017/S0022377825000054 Published online by Cambridge University Press